Lattice-Boltzmann simulation of creeping generalized Newtonian flows: theory and guidelines

Simon Gsell, Umberto d'Ortona, Julien Favier

Lattice-Boltzmann simulation of creeping generalized Newtonian flows: theory and guidelines

Simon Gsell[a,*], Umberto D'Ortona[a], Julien Favier[a]

[a] *Aix Marseille Univ, CNRS, Centrale Marseille, M2P2, Marseille, France*

Abstract

The accuracy of the lattice-Boltzmann (LB) method is related to the relaxation time controlling the flow viscosity. In particular, it is often recommended to avoid large fluid viscosities in order to satisfy the low-Knudsen-number assumption that is essential to recover hydrodynamic behavior at the macroscopic scale, which may in principle limit the possibility of simulating creeping flows and non-Newtonian flows involving important viscosity variations. Here it is shown, based on the continuous Boltzmann equations, that a two-relaxation-time (TRT) model can however recover the steady Navier-Stokes equations without any restriction on the fluid viscosity, provided that the Knudsen number is redefined as a function of both relaxation times. This effective Knudsen number is closely related to the previously-described parameter controlling numerical errors of the TRT model, providing a consistent theory at both the discrete and continuous levels. To simulate incompressible flows, the viscous incompressibility condition $Ma^2/Re \ll 1$ also needs to be satisfied, where Ma and Re are the Mach and Reynolds numbers. This concept is extended by defining a local incompressibility factor, allowing one to locally control the accuracy of the simulation for flows involving varying viscosities. These theoretical arguments are illustrated based on numerical simulations of the two-dimensional flow past a square cylinder. In the case of a Newtonian flow, the viscosity independence is confirmed for relaxation times up to 10^4, and the ratio $Ma^2/Re = 0.1$ is small enough to ensure reliable incompressible simulations. The Herschel-Bulkley model is employed to introduce shear-dependent viscosities in the flow. The proposed numerical strategy allows to achieve major viscosity variations, avoiding the implementation of artificial viscosity cut-off in high-viscosity regions. Highly non-linear flows are simulated over ranges of the Bingham number $Bn \in [1, 1000]$ and flow index $n \in [0.2, 1.8]$, and successfully compared to prior numerical works based on Navier-Stokes solvers. This work provides a general framework to simulate complex creeping flows, as encountered in many biological and industrial systems, using the lattice-Boltzmann method.

Keywords: lattice-Boltzmann, creeping flows, non-Newtonian flows

*Corresponding author, simon.gsell@univ-amu.fr

1. Introduction

The lattice-Boltzmann (LB) method is a popular method to simulate fluid flows [1, 2]. In contrast to Navier-Stokes methods which directly describe the dynamics of the macroscopic flow quantities (e.g. pressure, momentum), the LB method is a statistical approach based on gas kinetic theory. Originally derived from lattice-gaz models [3, 4], the LB method is a space-time discretization of the Boltzmann equation, which can recover the Navier-Stokes equations provided that the relevant conditions are satisfied [5, 6].

In many textbooks, the ability of the LB method to accurately predict macroscopic flow behaviors is assumed to rely on a small Knudsen number assumption, especially because this number is used as the expansion parameter in the Chapman-Enskog analysis, allowing to derive the Navier-Stokes equations from the Boltzmann equation [7]. The Knudsen number, denoted by Kn, is the ratio between the mean free path of gas particles and the typical length scale of the macroscopic problem, denoted by D in the following. It is often expressed using the von Kármán formulation, namely $Kn \sim Ma/Re$ [8], where Ma and Re are the Mach and Reynolds numbers of the physical system. The Mach number reads $Ma = u_0/c_s$, where u_0 is the typical flow velocity of the problem and c_s is the sound speed, which is set by the lattice in most LB implementations, unless a more generic method is used [9]. As the condition $Ma \ll 1$ must be satisfied to achieve incompressible flows, the condition $Kn \ll 1$ is simple to achieve in problems involving intermediate or large values of Re. In contrast, when $Re \ll 1$, the Mach number may have to be decreased, by decreasing the flow velocity u_0, in order to satisfy the low Knudsen assumption, resulting in higher computational costs. Due to this restriction, the lattice-Boltzmann method is not efficient in solving low Reynolds number (creeping) flows.

Alternatively, LB simulations of creeping flows can be performed by assuming the Stokes regime, where the flow is fully linear [10]. In this regime, the Reynolds number is not a physical parameter and it can thus be freely varied to satisfy the low Knudsen assumption. However, this approach requires an *a priori* assumption on the effect of flow inertia, which may not be obvious depending on the physical configuration [11]. In this work, a direct simulation approach is considered, where no assumption is made concerning the flow behavior, allowing one to perform simulations over a large range of Re including non-inertial and weakly-inertial flows.

In LB simulations, the fluid viscosity is controlled through a collision relaxation time, denoted by τ. Based on the kinematic viscosity $\nu = c_s^2(\tau - 1/2)$, the Reynolds number can be expressed as

$$Re = \frac{u_0 D}{c_s^2(\tau - 1/2)}. \tag{1}$$

Using the von Kármán formulation, the Knudsen number can thus be expressed as a function of the relaxation time, the sound speed and the macroscopic length scale,

$$Kn = \frac{c_s(\tau - 1/2)}{D}. \tag{2}$$

It appears that the Knudsen restriction is closely connected to the relaxation time τ: to achieve small Knudsen numbers, small values of τ and thus small fluid viscosities have to be

employed, if c_s and D are fixed. Note that in some LB implementations, c_s can be considered as a free parameter that is not connected to the fluid viscosity [9, 12, 10, 13]. Even though such an approach may allow small variations of Kn through c_s, the present work focuses on the dominant effect of τ, and c_s is kept constant as in common LB implementations [2, 1].

The analysis and correction of the effect of the fluid viscosity (or relaxation time) on the accuracy and stability of the lattice-Boltzmann method have motivated a number of works during last decades. Several approaches have been proposed to achieve viscosity independence of the simulations, especially by introducing multiple-relaxation-time collision models [14] with suitable scaling of the relaxation parameters [15, 9, 13]. The fluid viscosity may also greatly alter the accuracy of boundary conditions and immersed boundaries, which may require specific corrections [16]. In the two-relaxation-time (TRT) collision model [15, 17], symmetric and anti-symmetric parts of the distribution functions are relaxed at two different rates. While the first rate controls the kinematic viscosity, the second rate is not directly related to macroscopic properties and it can be freely varied to adapt the numerical accuracy. D'Humières and Ginzburg [17] showed that the numerical error can then become independent of the fluid viscosity if both relaxation rates satisfy a constant relation [17]. This result should allow one to employ large fluid viscosities to simulate low Reynolds number flows efficiently (see equation (1)). However, the *viscous* relaxation time must in principle remain limited by the above mentioned Knudsen restriction (see equation (2)). The present work aims at clarifying this aspect.

In addition to its impact on low Re simulations, the limitation of the relaxation time also questions the reliability of the LB method for the simulation of non-Newtonian flows. Viscoplastic fluids, as shear-thinning, shear-thickenning and yield-stress (or Bingham) fluids, are often modeled using shear-dependent viscosities, an approach referred to as generalized Newtonian modelling [18]. The LB method is a promising tool for the simulation of such flows, as it allows local computation of the flow shear rate using the distribution functions [19] and local variation of the fluid viscosity through the relaxation time [20, 21, 22, 23]. However, the resulting variation of the fluid viscosity raises the question of the relevant range of viscosities that can be covered while ensuring numerical accuracy. In particular, Bingham and shear-thinning fluids involve a major viscosity increase in low-shear regions of the flows. Even though the TRT lattice-Boltzmann model has already been successfully applied to Bingham flows in previous works [12, 24], general guidelines to design such simulations using LBM are still missing.

In this work, a detailed analysis of the TRT lattice-Boltzmann equation is presented in order to emphasize the impact of the physical and numerical parameters on the macroscopic flow behavior in the creeping regime, with a special attention paid to the effect of the relaxation times. A focus is placed on the steady case, as unsteady diffusive phenomena can not be accurately predicted at large viscosities using the LB method (see §2.4). The analysis shows that the Navier-Stokes equations can be recovered without any restriction on the fluid viscosity, Mach number, Reynolds number or nominal Knudsen number $Kn = Ma/Re$, provided that the physical Knudsen number is correctly redefined as a function of both relaxation times. The incompressible flow equations, however, can only be recovered if the viscous incompressibility factor $\mathcal{T} = Ma^2/Re$ is small. This result is verified numerically

based on the two-dimensional creeping flow past a square cylinder. This configuration is chosen as it involves non-trivial external flow dynamics while allowing accurate and simple implementation of the no-slip boundary conditions using the bounce-back method. In the case of a viscoplastic fluid modelled by the Herschel-Bulkley law, a local definition of the $\mathcal{T}$ criterion allows one to control the viscosity range of the flow solution and to achieve considerable viscosity ratios between low-shear and high-shear regions of the flow. The numerical results are discussed and compared to prior works based Navier-Stokes models.

The present paper is organized as follows. First, the lattice-Boltzmann method is briefly introduced in §2. Mesoscopic equations are then analyzed in §3, and the macroscopic flow equations are derived and discussed. The method is applied to the simulation of a Herschel-Bulkley flow past a square cylinder. The physical setup and the numerical implementation are first described in §4; the numerical results are then analyzed in §5. Finally, the principal conclusions of this work are summarized in a last section, in §6.

2. Lattice-Boltzmann method

The main aspects of the lattice-Boltzmann model employed in this work are presented in the following. After a brief presentation of the discrete-velocity Boltzmann equation in §2.1, the two-relaxation-time collision model is described in §2.2 and the space-time discretization leading to the LB equation is introduced in §2.3. The ability of the present method to simulate unsteady flows is discussed in §2.4.

2.1. Boltzmann equation and velocity discretization

The flow dynamics is described through the particle distribution function $f(\boldsymbol{x}, \boldsymbol{\xi}, t)$, representing the density of fluid particles moving with velocity $\boldsymbol{\xi}$, at location $\boldsymbol{x}$ and time t. The dynamics of the distribution function is governed by the Boltzmann equation,

$$\frac{\partial f}{\partial t} + \boldsymbol{\xi} \cdot \nabla f = \Omega(f), \tag{3}$$

where $\Omega(f)$ is the collision operator. The discretization of the Boltzmann equation in the velocity space, physical space, and time leads to the lattice-Boltzmann method.

The velocity space is discretized on a set of velocity vectors $\{\boldsymbol{c_i},\, i = 0, ..., Q-1\}$, where Q is the number of discrete velocities. In the present work, which only focuses on two-dimensional physical configurations, a $D2Q9$ velocity set is used. However, it should be mentioned that the following analysis does not rely on a particular velocity discretization. In the $D2Q9$ model, the velocity space is discretized on nine velocities, namely

$$\boldsymbol{c_i} = \begin{cases} (0,0), & i = 0, \\ c\left(\cos(\frac{\pi(i-1)}{2}), \sin(\frac{\pi(i-1)}{2})\right), & i \in [1,4], \\ \sqrt{2}c\left(\cos(\frac{\pi(2i-9)}{4}), \sin(\frac{\pi(2i-9)}{4})\right), & i \in [5,8], \end{cases} \tag{4}$$

where c is the lattice speed. The particle densities at velocities $\{\boldsymbol{c_i}\}$ are represented by the discrete-velocity distribution functions $\{f_i(\boldsymbol{x}, t)\}$, also called particle populations.

The macroscopic flow quantities are moments of the particle populations in the velocity space. In particular, the fluid momentum and density read

$$\rho \boldsymbol{u} = \sum_{i=0}^{8} f_i \boldsymbol{c_i}, \qquad \rho = \sum_{i=0}^{8} f_i, \tag{5}$$

with ρ and $\boldsymbol{u}$ the fluid density and velocity.

2.2. Two-relaxation-time Boltzmann equation

In the discretized velocity space $\boldsymbol{\xi} = \{\boldsymbol{c_i}\}$, the two-relaxation-time Boltzmann equation reads

$$\frac{\partial f_i}{\partial t} + \frac{\partial}{\partial x_\alpha}(c_{i,\alpha} f_i) = -\frac{1}{\tau^+}\left(f_i^+ - f_i^{eq+}\right) - \frac{1}{\tau^-}\left(f_i^- - f_i^{eq-}\right), \tag{6}$$

where τ^+ and τ^- are the two relaxation times and f_i^+ and f_i^- are symmetric and anti-symmetric parts of f_i, expressed as

$$f_i^+ = \frac{1}{2}(f_i + f_{\bar{i}}) \ ; \ f_i^- = \frac{1}{2}(f_i - f_{\bar{i}}), \tag{7}$$

with the index $\bar{i}$ defined so that $\boldsymbol{c_{\bar{i}}} = -\boldsymbol{c_i}$. When $\tau^+ = \tau^-$, equation (6) reduces to the single-relaxation-time (SRT) Boltzmann equation based on the Bhatnagar-Gross-Krook (BGK) collision operator [25].

Populations are decomposed into equilibrium and non-equilibrium parts, namely $f_i = f^{eq} + f^{neq}$. The equilibrium functions are expressed as

$$f_i^{(eq)} = w_i \rho \left(1 + \frac{\boldsymbol{u}\cdot\boldsymbol{c_i}}{c_s^2} + \frac{(\boldsymbol{u}\cdot\boldsymbol{c_i})^2}{2c_s^4} - \frac{\boldsymbol{u}\cdot\boldsymbol{u}}{2c_s^2}\right), \tag{8}$$

where c_s is the sound speed and $\{w_i\}$ are the lattice weights depending on the lattice model. In the case of the $D2Q9$ scheme, they read $w_0 = 4/9$, $w_1 = w_2 = w_3 = w_4 = 1/9$ and $w_5 = w_6 = w_7 = w_8 = 1/36$.

The symmetric and anti-symmetric populations exhibit a series of properties that are described in §Appendix A. These identities will be particularly useful when projecting the Boltzmann equation onto Hermite polynomials in §3.1.

2.3. Space-time discretization

Space-time discretization of the LB equation (6) is performed through a method of characteristics. It can be shown that the second-order discretized equation can be expressed in an explicit form, called the lattice-Boltzmann equation, namely [2]

$$\hat{f}_i(\boldsymbol{x} + \boldsymbol{c_i}\Delta t, t + \Delta t) - \hat{f}_i(\boldsymbol{x}, t) = -\frac{1}{\hat{\tau}^+}\hat{f}_i^{neq+} - \frac{1}{\hat{\tau}^-}\hat{f}_i^{neq-}, \tag{9}$$

through the change of variable

$$\hat{f}_i = f_i + \frac{1}{2}\left(\frac{1}{\tau^+} f_i^{neq+} + \frac{1}{\tau^-} f_i^{neq-}\right), \tag{10}$$

and defining $\hat{f}_i^+ = (\hat{f}_i + \hat{f}_{\bar{i}})/2$ and $\hat{f}_i^- = (\hat{f}_i - \hat{f}_{\bar{i}})/2$, and the numerical relaxation times $\hat{\tau}^+ = \tau^+ + 1/2$ and $\hat{\tau}^- = \tau^- + 1/2$, with $\tau^\pm > 0$ and $\hat{\tau}^\pm > 1/2$.

Equation (9) is defined on a two-dimensional uniform and Cartesian grid which consists of a series of nodes spaced by a distance Δn in the x and y directions. This lattice satisfies the acoustic scaling condition $c = \Delta n/\Delta t$, where Δt is the numerical time step. Therefore, the streaming process, on the left-hand side of equation (9), is characterized by the transport of the populations from one node to a neighboring one at the lattice speed c. It is balanced by the collision process, on the right-hand side of the equation.

D'Humières and Ginzburg [17] have shown that the discretization errors on steady-state bulk solutions and specific boundary rules are controlled by an effective relaxation time, also called *magic* collision parameter, $\Lambda = (\hat{\tau}^+ - 1/2)(\hat{\tau}^- - 1/2)$. Small discretization errors are generally expected for values of Λ close to 0.1 [2]. In particular, the value $\Lambda = 1/4$ ensures optimal stability conditions [26, 27].

2.4. From unsteady to steady Boltzmann equations

The TRT Boltzmann equation (6), or its discretized counterpart (9), are not suitable to describe highly viscous unsteady flows. As shown in the following, the fluid viscosity is determined by the relaxation time τ^+, namely $\nu = c_s^2\tau^+$, where ν is the kinematic viscosity. A typical numerical time scale related to viscous diffusion can thus be expressed as $t_\nu = \Delta n^2/\nu = 3/\tau^+$, using the lattice scaling $\Delta n = \Delta t = 1$ and $c_s = 1/\sqrt{3}$. In order to accurately describe unsteady diffusive phenomena, the diffusive time scale should be larger than numerical time step, namely $t_\nu > 1$. In theory, this condition is only satisfied when $\tau^+ < 3$. Even though in practice this critical value may vary from one case to the other, this condition illustrates that the lattice-Boltzmann method is generally not reliable for the simulation of highly viscous unsteady flows involving large values of the relaxation time.

Other time integration strategies, as dual-time-stepping approaches [28], can be employed to simulate highly viscous unsteady flows using the lattice-Boltzmann method. This method relies on the accuracy of the lattice-Boltzmann in simulating steady fluid flows. Therefore, in the following the focus is first placed on the analysis of the steady TRT-LB method. The simulation of unsteady flows will be addressed in a future work.

Here, the unsteady LB equation is thus only employed as a method to reach steady flow solutions. The transient part of the simulations is ignored, and a focus is placed on the reliability of the obtained steady solutions. Once a steady solution is reached, the system satisfies the steady TRT lattice-Boltzmann equation. Its continuous counterpart is the steady Boltzmann equation, which is obtained by ignoring the time derivative in equation (6),

$$\frac{\partial}{\partial x_\alpha}(c_{i,\alpha} f_i) = -\frac{1}{\tau^+}\left(f_i^+ - f_i^{eq+}\right) - \frac{1}{\tau^-}\left(f_i^- - f_i^{eq-}\right). \tag{11}$$

3. Analysis of the steady TRT Boltzmann equation

In the following, the steady TRT Boltzmann equation is analyzed in order to characterize the emerging macroscopic flow behavior, especially in the viscous flow regime. The analysis is based on the velocity-discretized Boltzmann equation (11), in order to ignore numerical errors related to the space-time discretization, which have already been thoroughly examined in prior works [17].

3.1. Hermite projection of the Boltzmann equation

To recover the macroscopic equations, equation (11) is projected onto Hermite polynomials of increasing order, through the discrete operator

$$< f_i|\boldsymbol{\mathcal{H}}_i^{(n)} >= \sum_i f_i \boldsymbol{\mathcal{H}}_i^{(n)}, \tag{12}$$

where $\boldsymbol{\mathcal{H}}^{(n)}$ is the n-rank Hermite tensor. Hermite tensors from order $n = 0$ to order $n = 2$ can be expressed as [29]

$$\mathcal{H}_i^{(0)} = 1, \qquad \mathcal{H}_{i,\alpha}^{(1)} = c_{i,\alpha}, \qquad \mathcal{H}_{i,\alpha\beta}^{(2)} = c_{i,\alpha}c_{i,\beta} - c_s^2\delta_{\alpha,\beta}. \tag{13}$$

It should be noted that the following analysis is based on the equilibrium distribution functions defined by equation (8), that are already truncated in the Hermite space. Indeed, this analysis only aims at deriving the macroscopic equations recovered by the present LB model, and the effect of Hermite truncation is not directly addressed.

At order 0, the Boltzmann equation (11) recovers the mass equation,

$$\frac{\partial}{\partial x_\alpha}(\rho u_\alpha) = 0. \tag{14}$$

Then the first-order projection,

$$\frac{\partial}{\partial x_\alpha}(\sum_i f_i c_{i,\alpha}c_{i,\beta}) = 0, \tag{15}$$

involves the second-order moment $\Pi_{\alpha\beta} = \sum_i f_i c_{i,\alpha}c_{i,\beta}$. Its equilibrium part $\Pi_{\alpha\beta}^{eq} = \sum_i f_i^{eq} c_{i,\alpha}c_{i,\beta}$ can be directly computed from the expression of f_i^{eq} ; it reads $\Pi_{\alpha\beta}^{eq} = \rho c_s^2\delta_{\alpha\beta} + \rho u_\alpha u_\beta$. Expression (15) thus becomes

$$\frac{\partial}{\partial x_\alpha}(\rho c_s^2\delta_{\alpha\beta} + \rho u_\alpha u_\beta) + \frac{\partial}{\partial x_\alpha}(\sum_i f_i^{neq} c_{i,\alpha}c_{i,\beta}) = 0. \tag{16}$$

Expression (16) governs the flow momentum transport. The first term of the equation relates to inviscid fluxes. The flow pressure can be identified by introducing the isothermal ideal gaz state equation, $p = \rho c_s^2$. However, the non-equilibrium second-order moment, $\Pi_{\alpha\beta}^{neq} = \sum_i f_i^{neq} c_{i,\alpha}c_{i,\beta}$, remains to be determined. In order to recover a hydrodynamic behavior, $\Pi_{\alpha\beta}^{neq}$ should be equal to the viscous stress tensor.

The tensor $\Pi^{neq}_{\alpha\beta}$ can be explicitly computed by performing a second-order projection of the Boltzmann equation, as detailed in Appendix B. The resulting equation reads

$$2\rho c_s^2 S_{\beta\gamma} + \frac{\partial}{\partial x_\alpha}(\mathcal{Q}^{neq}_{\alpha\beta\gamma}) - u_\gamma \frac{\partial}{\partial x_\alpha}(\Pi^{neq}_{\alpha\beta}) - u_\beta \frac{\partial}{\partial x_\alpha}(\Pi^{neq}_{\alpha\gamma}) = \frac{-\Pi^{neq}_{\beta\gamma}}{\tau^+}, \tag{17}$$

where $\mathcal{Q}_{\alpha\beta\gamma}$ is the third-order moment defined by $\mathcal{Q}_{\alpha\beta\gamma} = \sum_i f_i c_\alpha c_\beta c_\gamma$ and $S_{\alpha\beta} = \frac{1}{2}\left(\frac{\partial u_\alpha}{\partial x_\beta} + \frac{\partial u_\beta}{\partial x_\alpha}\right)$ is the shear-rate tensor. The viscous stress tensor can be recognized in the first term of equation (17). However, other terms represent non-hydrodynamic contributions to the macroscopic flow behavior. These terms are quantified hereafter following the Chapman-Enskog procedure.

3.2. Chapman-Enskog expansion

The distribution functions are expanded around the equilibrium solution $f_i = f_i^{eq}$ using the expansion parameter $\epsilon \ll 1$, namely

$$f_i = \sum_{n=0}^{N} \epsilon^n f_i^{(n)}, \tag{18}$$

where N is the order of the expansion. The definition of the expansion parameter ϵ will be discussed in the next section. At order 0, the distribution functions are equal to the equilibrium distributions, $f_i^{(0)} = f_i^{eq}$. The multi-scale expansion consists in substituting this expansion in the Boltzmann equation and projecting the equation on different orders of ϵ. The space derivative is considered to be first order, and expanded in the form $\frac{\partial}{\partial x} = \epsilon \frac{\partial}{\partial x}^{(1)}$. If ϵ is small enough, f_i can be reasonably approximated by $f_i \approx f_i^{eq} + \epsilon f^{(1)}$. By expanding the shear-rate tensor as $S_{\beta\gamma} = \epsilon S^{(1)}_{\beta\gamma}$, expression (17) becomes

$$\epsilon\Pi^{(1)}_{\beta\gamma} = -2\tau^+\rho c_s^2 \epsilon S^{(1)}_{\beta\gamma} - \epsilon^2\tau^+ \frac{\partial^{(1)}}{\partial x_\alpha}(Q^{(1)}_{\alpha\beta\gamma}) + u_\gamma\tau^+\epsilon^2 \frac{\partial^{(1)}}{\partial x_\alpha}(\Pi^{(1)}_{\alpha\beta}) + u_\beta\tau^+\epsilon^2 \frac{\partial^{(1)}}{\partial x_\alpha}(\Pi^{(1)}_{\alpha\gamma}), \tag{19}$$

which at first order reduces to

$$\epsilon\Pi^{(1)}_{\beta\gamma} = -2\tau^+\rho c_s^2 \epsilon S^{(1)}_{\beta\gamma}, \tag{20}$$

or, reversing the spatial derivative expansion,

$$\Pi^{neq}_{\beta\gamma} = -2\tau^+\rho c_s^2 S_{\beta\gamma}. \tag{21}$$

Substituting $\Pi^{neq}_{\beta\gamma}$ in the momentum equation (16) finally gives the expected steady momentum equation. By adding the mass equation (14), the Navier-Stokes equations are obtained,

$$\frac{\partial}{\partial x_\alpha}(\rho u_\alpha) = 0, \tag{22a}$$

$$\frac{\partial}{\partial x_\beta}(\rho u_\alpha u_\beta) = -\frac{\partial p}{\partial x_\alpha} + \frac{\partial}{\partial x_\beta}(2\mu S_{\alpha\beta}), \tag{22b}$$

with $p = \rho c_s^2$ and $\mu = \rho c_s^2 \tau^+$. The relaxation time τ^+, which controls the fluid viscosity, is called the *viscous* relaxation time in the following. In contrast, τ^- is not involved in the macroscopic equations; it is called the *free* relaxation time. Note that in the above analysis, no assumption has been made concerning the *viscous* relaxation time τ^+; in particular, τ^+ can be space dependent [2]. The definition $\mu = \rho c_s^2 \tau^+$ thus applies to non-uniform viscosities, e.g. shear-dependent viscosities, as already done in prior works [12, 24].

The above Chapman-Enskog analysis is equivalent for both the single- and two-relaxation-time collision models, since the multi-scale expansion only has to be performed on the second-order projection of the Boltzmann equation (17), which only involves the *viscous* relaxation time. Therefore, both models may appear to be equivalent at the macroscopic level. In both cases, the derived hydrodynamic equations (22) rely on the small value of the expansion coefficient ϵ, as all terms $\sim \mathcal{O}(\epsilon^2)$ have been neglected. If $\epsilon \ll 1$ is not satisfied, additional macroscopic equations can emerge and lead to non-hydrodynamic behaviors, e.g. visco-elastic effects [30]. The definition of ϵ is thus crucial to close the analysis. As discussed in the following, this aspect reveals important differences between the SRT and TRT models.

3.3. Discussion on the Knudsen number

The Chapman-Enskog expansion aims at expressing deviations from the equilibrium solution through small perturbations whose amplitude is quantified by the expansion parameter ϵ. Therefore, this parameter controls the magnitude of the non-equilibrium functions; in particular, $f_i^{neq} = 0$ must be satisfied when $\epsilon = 0$. In the case of the SRT collision model, the solution tends to the equilibrium distribution when the relaxation time tends to 0. Therefore, τ^+ can be employed as a perturbative parameter, namely $\epsilon_{SRT} \sim \tau^+$. Generally, the expansion parameter is rather expressed as a Knudsen number Kn, quantifying the ratio between the molecular free path length l and the typical hydrodynamic length scale D. The Knudsen number can be determined based on the Reynolds Re and Mach Ma numbers through the von Kármán relation, namely $Kn = Ma/Re$, which can be re-written as $Kn = \tau^+ c_s / D$. If the value of c_s is fixed by the lattice as in the present LB model, it is seen that both definitions $\epsilon_{SRT} \sim \tau^+$ or $\epsilon_{SRT} \sim Kn$ are equivalent for a given value of D. The Chapman-Enskog expansion can only be performed if $Kn \ll 1$; consequently, the SRT lattice-Boltzmann method only recovers the Navier-Stokes equations for low Knudsen number configurations. The relation $\epsilon \sim \tau^+$ clearly indicates the limitation of the SRT collision model: the *viscous* relaxation time, i.e. the fluid viscosity, has an influence on the resulting macroscopic equations, since large relaxation times (or large Kn) will result in the growth of non-hydrodynamic modes in the momentum equation (17).

The definition $\epsilon \sim \tau^+$ can not be employed in the case of the TRT collision model, since both τ^+ and τ^- are expected to impact the magnitude of the non-equilibrium functions. The relevant expansion parameter can be determined by expressing the non-equilibrium populations as functions of both relaxation times, as detailed in Appendix C. This analysis shows that, in the case of the TRT collision model, the equilibrium solution is achieved when the product of both relaxation times tends to 0, namely $\tau^+ \tau^- \to 0$. Note that this result holds for continuous equations, as additional terms may emerge at the discrete level. The parameter $\epsilon_{TRT} \sim \sqrt{\tau^+ \tau^-}$ can thus be considered as a relevant parameter for the

expansion. Interestingly, this number is equivalent to the *magic* collision number $\Lambda = \tau^+\tau^-$, identified by d'Humières and Ginzburg [17], that determines the magnitude of the numerical errors of the TRT lattice-Boltzmann equation, i.e. the TRT Boltzmann equation (11) after spatial discretization. Here, it is proposed to express it as an effective Knudsen number, $Kn^* = \sqrt{\tau^+\tau^-}c_s/D = \sqrt{\Lambda}c_s/D$, corresponding to the relevant expansion parameter for the Chapman-Enskog analysis of both the SRT and TRT Boltzmann equations.

The Knudsen number controls the reliability of the Boltzmann equation in modeling fluid flows, as it determines the magnitude of high-order non-hydrodynamic terms in the expression of the shear-stress tensor (see equation (19)). Small values of Kn^* should therefore be used in LB simulations. Using a SRT collision model, small Knudsen numbers can only be achieved by choosing small relaxation times, i.e. by performing weakly viscous simulations. In contrast, the TRT model allows one to freely increase the *viscous* relaxation time, provided that $\tau^+\tau^-$ remains small. This property, already established based on the space-discretized equations [17], is supported by the present continuous analysis, providing a consistent theory at both the discrete and continuous levels.

3.4. Non-dimensional macroscopic equations and incompressibility assumption

Generally, a hydrodynamic problem described by the Navier-Stokes equations (22) is expected to depend at least on five physical parameters, namely a reference density ρ_0, a reference velocity u_0, a reference kinematic viscosity (or relaxation time) $\nu_0 = c_s^2\tau_0^+$, the speed of sound c_s and a reference length scale D. Following the Buckingham theorem, the non-dimensional flow solution should only depend on two non-dimensional parameters, that are often defined as the Reynolds number Re and Mach number Ma,

$$Re = \frac{u_0 D}{\nu_0}, \qquad Ma = \frac{u_0}{c_s}. \tag{23}$$

For inertial flows, a set of non-dimensional physical quantities can be defined as $\boldsymbol{u}^* = \boldsymbol{u}/u_0$, $\rho^* = c_s^2(\rho - \rho_0)/\rho_0 u_0^2$, $\nu^* = \nu/\nu_0$ and $\boldsymbol{S}^* = \boldsymbol{S}D/u_0$. The non-dimensional flow equations read

$$\nabla \cdot (\boldsymbol{u}^*) + Ma^2 \nabla \cdot (\rho^* \boldsymbol{u}^*) = 0, \tag{24a}$$

$$\nabla \cdot (\boldsymbol{u}^*\boldsymbol{u}^*) + Ma^2 \nabla \cdot (\rho^* \boldsymbol{u}^*\boldsymbol{u}^*) = -\nabla(\rho^*) + \frac{2}{Re}\nabla \cdot (\nu^* \boldsymbol{S}^*) + \frac{2}{Re} Ma^2 \nabla \cdot (\rho^* \nu^* \boldsymbol{S}^*). \tag{24b}$$

If the Mach number is small enough, these equations recover the steady incompressible Navier-Stokes equations,

$$\nabla \cdot (\boldsymbol{u}^*) = 0, \tag{25a}$$

$$\nabla \cdot (\boldsymbol{u}^*\boldsymbol{u}^*) = -\nabla(\rho^*) + \frac{2}{Re}\nabla \cdot (\nu^* \boldsymbol{S}^*). \tag{25b}$$

Note that $\nu^* = 1$ in the Newtonian case.

Alternatively, if the flow is expected to be dominated by viscous stresses, as in the present study, the non-dimensional density should be defined as $\hat{\rho}^* = c_s^2(\rho - \rho_0)D/\mu_0 u_0$. A different set of non-dimensional equations is then obtained,

$$\nabla \cdot (\boldsymbol{u}^*) + \frac{Ma^2}{Re}\nabla \cdot (\hat{\rho}^* \boldsymbol{u}^*) = 0, \tag{26a}$$

$$Re\nabla \cdot (\boldsymbol{u}^*\boldsymbol{u}^*) + Ma^2\nabla \cdot (\hat{\rho}^*\boldsymbol{u}^*\boldsymbol{u}^*) = -\nabla(\hat{\rho}^*) + 2\nabla \cdot (\nu^* \boldsymbol{S}^*) + 2\frac{Ma^2}{Re}\nabla \cdot (\hat{\rho}^*\nu^*\boldsymbol{S}^*). \tag{26b}$$

In this case, the incompressible Navier-Stokes equations (25) are recovered if the Mach and Reynolds numbers satisfy $Ma^2 \ll Re$, or equivalently $\mathcal{T} = Ma^2/Re = \tau_0^+ u_0/D \ll 1$, where $\mathcal{T}$ is the viscous incompressibility factor.

In summary, the above theoretical analysis indicates that highly viscous flow simulations can be performed using the proposed TRT-LB method, provided that the effective Knudsen number $Kn^* = \sqrt{\tau_0^+\tau_0^-}c_s/D = \sqrt{\Lambda}c_s/D$ and the viscous incompressibility factor $\mathcal{T} = Ma^2/Re$ are small enough. These features are numerically investigated in the following on the basis of simulations of the flow past a square cylinder.

4. Physical and numerical setup

The theoretical analysis developed in §3 is applied in the following to the simulation of the flow past a square cylinder. Complex fluids are described using a Non-Newtonian Herschel-Bulkley model, described in §4.1. Details on the physical setup are presented in §4.2, and the numerical parameters are discussed in §4.3.

4.1. Non-Newtonian Herschel-Bulkley model

The Herschel-Bulkley model is employed to simulate non-Newtonian flows of viscoplastic fluids. The local dynamic fluid viscosity follows

$$\mu = \frac{\sigma_0}{\dot{\gamma}} + k\dot{\gamma}^{n-1}, \tag{27}$$

where σ_0 is the yield stress, k is the flow consistency, n is the flow index, $\dot{\gamma}$ is the local shear-rate magnitude, expressed as [22, 31, 32, 33, 34]

$$\dot{\gamma} = \sqrt{2\boldsymbol{S} : \boldsymbol{S}}, \tag{28}$$

and $\boldsymbol{S}$ is the shear-rate tensor. When the fluid is Newtonian, $\sigma_0 = 0$ and $n = 1$, thus the fluid viscosity is equal to the fluid consistency. When $n < 1$, the fluid exhibits a shear-thinning behavior, i.e. its viscosity decreases as a function of the shear rate. The opposite trend, when $n > 1$, is called shear-thickening behavior. The yield stress introduces a rapid variation of the viscosity as the shear rate approaches σ_0/μ_0. This behavior aims at reproducing the shear-dependent *solid*/*fluid* transitions observed in many complex flows. The *solid*-like behavior is thus modeled by an infinitely large viscosity.

In practice, the local fluid viscosity is varied through the *viscous* relaxation time $\hat{\tau}^+$,

$$\hat{\tau}^+ = \frac{1}{2} + \frac{\mu}{\rho c_s^2}. \tag{29}$$

The value of μ is determined by computing the local shear-rate tensor based on the non-equilibrium distribution functions, following equation (21),

$$\boldsymbol{S} = -\frac{1}{2\rho c_s^2 \hat{\tau}^+} \sum_{i=1}^{8} \left(f_i - f_i^{(eq)} \right) \boldsymbol{c_i c_i}. \tag{30}$$

As $\hat{\tau}^+$ is involved in the expression of $\boldsymbol{S}$, the value of $\hat{\tau}^+$ from the previous time step is used. This has no effect of the numerical results since only steady solutions are considered in this work.

In many numerical works, the Herschel-Bulkley law is truncated in order to avoid excessive viscosities in the computational domain that may deteriorate the numerical stability and accuracy. Regularized viscosity models have been proposed to achieve this truncation while avoiding sharp transitions between truncated and non-truncated regions [35]. The effect of this regularization has been analyzed in prior works [12, 36]. Here, an original Herschel-Bulkley law without truncation is employed, taking advantage of the viscosity-independence of the present numerical framework. However, the viscosity remains restricted by the floating point approximation and thus it can not reach infinite values. In particular, the shear-rate $\dot{\gamma} = 0$ must be avoided in expression (27). In practice, the maximum value of the viscosity is thus set by controlling the minimum shear-rate value in expression (27), by redefining $\dot{\gamma}$ as $\dot{\gamma} \leftarrow \max(\dot{\gamma}, \epsilon_{\dot{\gamma}})$, with $\epsilon_{\dot{\gamma}} = 10^{-14}$.

4.2. Physical setup

The physical configuration is schematized in figure 1. A square cylinder of size D is immersed in an oncoming flow characterized by its velocity u_0, density ρ_0, consistency k, flow index n and yield stress σ_0. A square computational domain is used; its size is denoted by L. The flow inlet is set by a velocity Dirichlet condition based on the bounce-back method. The density at the boundary is set to the reference velocity ρ_0. At the outlet, a pressure Dirichlet condition is ensured through a non-equilibrium bounce-back method. The boundary density and tangential velocity are set to ρ_0 and 0, and the normal flow velocity is derived from density and momentum balance [37]. Periodic boundary conditions are set on the upper and lower boundaries. Finally, the no-slip condition on the square cylinder is enforced by a halfway bounce-back method.

While the bounce-back method is expected to achieve viscosity-independent numerical errors at the boundary [15, 17], ensuring an accurate solution at the cylinder surface, the viscosity independence is not theoretically ensured at the outlet where the non-equilibrium bounce-back approach is applied. However, this boundary has a smaller effect on the overall flow as it is placed far from the cylinder. In practice, a good viscosity-independence of the flow solution close to the cylinder is obtained in the present simulations, as illustrated in the following.

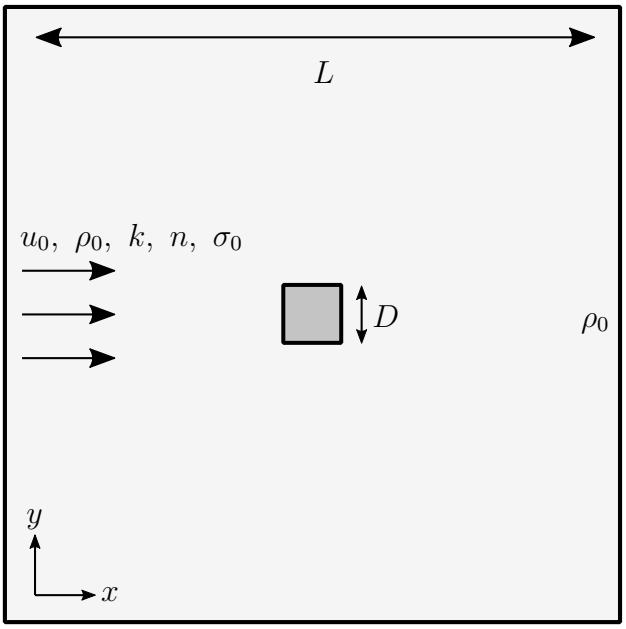

Figure 1: Schematic view of the physical configuration: a square cylinder of size D is immersed in a flow characterized by its velocity u_0, density ρ_0, consistency k, flow index n and yield stress σ_0.

Several non-dimensional numbers can be defined to characterize the physical setup. First, the Reynolds number reads

$$Re = \frac{\rho_0 u_0 D}{\mu_0}, \tag{31}$$

where μ_0 is the reference viscosity. It is associated with a reference *viscous* relaxation time $\hat{\tau}_0^+$. If the fluid is Newtonian or if it is a Bingham fluid ($n = 1$ and $\sigma_0 \geq 0$), the reference viscosity is equal to the fluid consistency, $\mu_0 = k$. When $n \neq 1$, the reference viscosity depends on the physical configuration. A reference shear rate can be defined as $\dot{\gamma}_0 = u_0/D$, allowing one to derive the reference viscosity $\mu_0 = k\dot{\gamma}_0{}^{n-1}$. Overall, the general definition of the Reynolds number is [36]

$$Re = \frac{\rho_0 u_0^{2-n} D^n}{k}. \tag{32}$$

Then, the Bingham number,

$$Bn = \frac{\sigma_0}{k}\left(\frac{D}{u_0}\right)^n, \tag{33}$$

is used to quantify the ratio between the yield stress and the viscous stresses in the flow.

The drag force exerted by the fluid on the body is used to examine the accuracy of the numerical simulations. The drag force is often normalized by the reference inertial stress to define the drag coefficient,

$$C_x = \frac{2F_x}{\rho_0 u_0^2 D}, \tag{34}$$

where F_x is the fluid force in the x direction. However, when the flow is governed by viscous stresses, it is more convenient to define another coefficient, referred to as viscous drag coefficient in the following,

$$C_{x,\mu} = C_x Re = \frac{2F_x}{k u_0^n D^{1-n}}. \tag{35}$$

Finally, a third definition should be introduced when a creeping flow is dominated by the yield stress σ_0 at large Bingham numbers, namely

$$C_{x,\sigma_0} = \frac{C_x Re}{Bn} = \frac{2F_x}{\sigma_0 D}. \tag{36}$$

In the present LB implementation, the fluid force $\boldsymbol{F} = (F_x, F_y)$ exerted on the cylinder is determined through a momentum balance approach. Considering a surface Γ encompassing the cylinder, the fluid force is balanced, when the steady solution is reached, by the integrated stresses on Γ, namely

$$\boldsymbol{F} + \int_\Gamma \boldsymbol{\sigma} \cdot \boldsymbol{n} dS = 0, \tag{37}$$

where $\sigma = -p\boldsymbol{I} + 2\mu\boldsymbol{S}$ is the stress tensor, $\boldsymbol{I}$ is the unit tensor and $\boldsymbol{n}$ is the unit normal vector on Γ. Note that the shear-rate tensor $\boldsymbol{S}$ is computed locally using expression (30). The force $\boldsymbol{F}$ is determined at each time step using equation (37), after the update of the macroscopic quantities.

4.3. Numerical parameters

The theoretical analysis performed in §3 has shown that a number of numerical parameters has to be carefully set in order to ensure the reliability of the simulations. First, the two relaxation times $\hat{\tau}^+$ and $\hat{\tau}^-$ have to be chosen so that the effective Knudsen number Kn^* remains small. In practice, this is achieved by setting the relaxation time product $\Lambda = (\hat{\tau}^+ - 1/2)(\hat{\tau}^- - 1/2)$ to a constant value, equal to $1/6$ in the following. This value has been reported to be optimal for diffusive problems [2] and it keeps Kn^* to a reasonably small value: $Kn^* = \sqrt{\Lambda} c_s / D$ remains lower than 0.01 as long as the cylinder size D is larger than $10\Delta n$. In non-Newtonian simulations, the *free* relaxation time $\hat{\tau}^-$ is thus varied together with $\hat{\tau}^+$ in order to maintain the constant value of Λ.

Then, the viscous incompressibility factor $\mathcal{T} = Ma^2/Re$, with $Ma = u_0/c_s$, is set to control the incompressibility of the flow. If the value of the Reynolds number is fixed, $\mathcal{T}$ determines the reference velocity u_0 which drastically impacts the computational cost: when the flow velocity is decreased, transient simulations get longer and more time steps have to be performed to reach a steady solution. The optimal value of $\mathcal{T}$ will be discussed in §5.

When the fluid is non-Newtonian, the local viscosity varies across the computational domain. This variation may be seen as a variation of the local Reynolds number, which in turn alters the incompressibility factor. The local Reynolds number is defined as the local ratio between inertial and viscous stresses, expressed as

$$Re_l = \frac{\rho |\boldsymbol{u}|^2}{\mu \dot{\gamma}}, \tag{38}$$

where $|\boldsymbol{u}|$ is the local velocity magnitude. A local Mach Number is also defined as $Ma_l = |\boldsymbol{u}|/c_s$. Consequently, the local incompressibility factor reads

$$\mathcal{T}_l = \frac{\mu\dot{\gamma}}{\rho c_s^2}. \tag{39}$$

According to the previous analysis, the fluid viscosity has no influence on the simulation accuracy as long as the incompressibility factor is small enough. Therefore, the local quantity $\mathcal{T}_l$ is employed to control the variation of the viscosity and ensure the simulation reliability. Given a maximum value of $\mathcal{T}_l$ that is acceptable to satisfy the incompressibility condition, called $\mathcal{T}_{max}$, the local maximum fluid viscosity is defined as $\mu_{max} = \mathcal{T}_{max}\rho c_s^2/\dot{\gamma}$. Following this procedure, it is seen that μ_{max} tends to infinity when the shear rate tends to zero, which is expected to allow major viscosity variations in the simulations. In practice, when μ_{max} is reached during a simulation, the Herschel-Bulkley law is artificially truncated, altering the accuracy of the non-Newtonian modelling. In this case, the reference incompressibility factor $\mathcal{T}$ can be further decreased until the whole flow solution satisfies the incompressibility condition, reproducing a realistic Herschel-Bulkley law without any cut-off and achieving major viscosity ratios across the computation domain.

5. Numerical results

The reliability of the present numerical method for the simulation of creeping non-Newtonian flows is examined in the following. First, a series of simulations is performed for intermediate values of the Reynolds number ($Re \geq 1$) in order to set the grid resolution and illustrate the reliability of the method in this well-documented flow regime; these results are presented in §5.1. Then, the creeping flow regime ($Re \ll 1$) is explored in §5.2, in particular to demonstrate the viscosity independence of the present numerical strategy. The method is then applied to viscoplastic fluids, namely yield-stress fluid in §5.3 and shear-thinning and shear-thickening fluids in §5.4.

5.1. Validation results at $Re \geq 1$

Figure 2(a) shows the evolution of the drag force coefficient as a function of the mesh refinement, quantified by $D/\Delta n$. The Reynolds number is set to $Re = 1$ and the size of the computational domain is $L = 50D$. A clear converging trend is noted, although the overall variation of C_x remains small over the considered range of $D/\Delta n$. Indeed, it should be noted that the relative amplitude of the C_x axis in this plot is only about 5%. The influence of the domain size on the drag force coefficient at $Re = 1$ is examined in figure 2(b), for $D/\Delta n = 5$. The domain size significantly impacts C_x, even when large domains are used, as expected due to the low value of the Reynolds number.

In the following, the domain size is limited in order to keep a reasonable computational cost and allow some parametric analyses. It should be mentioned that, as confinement effects are expected to increase as the Reynolds number decreases, the following simulations performed for $Re \ll 1$ are necessarily expected to be altered by the domain size, unless a very large domain is used [39]. Convergence regarding this parameter is thus not required

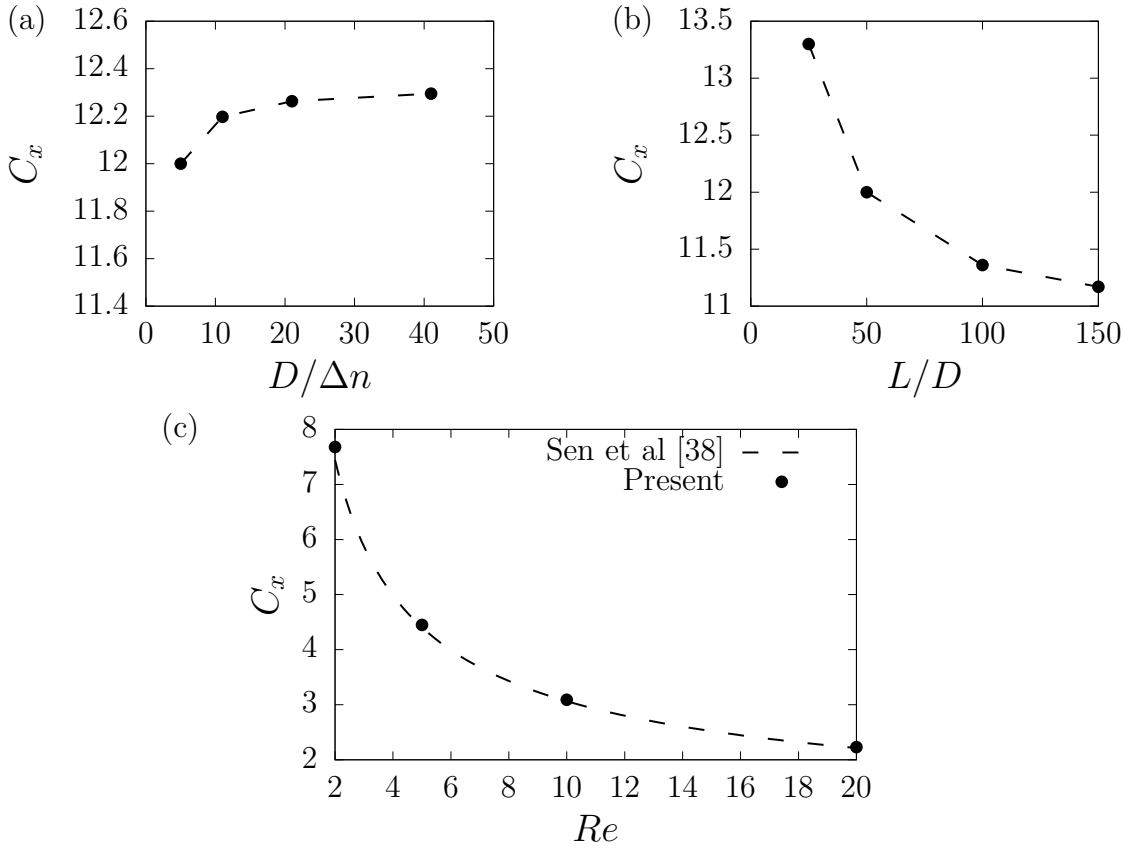

Figure 2: Flow past a square cylinder for $Re \geq 1$: evolution of the drag force coefficient C_x as a function of (a) the mesh resolution $D/\Delta n$ and (b) domain size L/D for $Re = 1$, and (c) as a function of the Reynolds number for $D = 21\Delta n$ and $L = 50D$.

in this study. An intermediate domain size, avoiding strong interactions between boundary layers close to the body and the domain boundaries, while limiting the computational cost, is employed in the following. The reference numerical setup is chosen as $D = 21\Delta n$ and $L = 50D$. These parameters allow a reasonably accurate prediction of the flow in the range $Re \in [2, 20]$, as depicted in figure 2(c). Values of the drag coefficient are compared to the empirical drag law proposed by Sen et al. [38] based on high-definition finite-element simulations over the range $Re \in [2, 40]$, expressed as

$$C_x = 0.7496 + 10.5767 Re^{-0.66}. \tag{40}$$

This value of the drag force corresponds to simulations involving negligible blockage effects. It is seen in figure 2(c) that the present numerical setup accurately reproduces this drag evolution.

In addition, as described in §5.3 and §5.4, the present numerical framework leads to accurate flow predictions in configurations involving viscoplastic fluids. The effect of the domain size, which varies as a function of fluid properties, is also further discussed in the following.

5.2. Creeping Newtonian flow past a square cylinder

The reliability of the present numerical framework in simulating highly viscous flows is examined in the following, in the case of a Newtonian fluid. Figure 3(a) shows the predicted drag force coefficient $C_{x,\mu} = C_x Re$ for two Reynolds numbers, $Re = 10^{-2}$ and $Re = 10^{-3}$, over a range of the incompressibility factor $\mathcal{T}$. In order to keep the Reynolds number constant, $\mathcal{T}$ is varied together with the *viscous* relaxation time τ^+ and Mach number Ma. This procedure drastically impacts the computational efficiency, since more time steps have to be performed to achieve steady flow solutions when the flow velocity is reduced. According to the analysis performed in §3, $\mathcal{T}$ should be the only numerical parameter impacting the simulations, and numerical accuracy should be ensured as long as $\mathcal{T} \ll 1$. This is supported by the results in figure 3(a), where the drag coefficient exhibits a converging trend as the incompressibility factor is decreased. The constant value of $C_{x,\mu}$ in the range $\mathcal{T} \ll 1$ indicates that other numerical parameters, in particular the *viscous* relaxation time, have no effect on the simulation result. Numerical simulations are considered to be reliable in this range, where numerical parameters approach their *regular* values, namely $\hat{\tau}^+ \sim 1$, $Ma \ll 1$ and $Kn \ll 1$ (see table 1 described hereafter).

Some additional simulations have been performed using a domain length $L = 100D$ to allow quantitative comparison with the numerical data reported by Pantokratoras[39] based on this particular geometry. In this configuration, for $Re = 0.01$, the drag predicted by the present method $C_{x,\mu} = 6.74$ is comparable to the value of 7.2 reported in that paper. Small differences between both simulations may however be due to the employed boundary conditions, since velocity Dirichlet conditions are set on the upper and lower boundaries of the domain in Pantokratoras' simulations, and thus the confinement conditions differ between both studies. Further comparison with the data issued from that study, including a discussion on the domain boundary effects, will be presented in §5.4.

Values of $C_{x,\mu}$ are very similar for both values of the Reynolds number, suggesting that the creeping flow regime $Re \approx 0$ is reached. The relative variation of $C_{x,\mu}$ when $\mathcal{T}$ is varied from 0.001 to 0.1 is lower than 1%. Therefore, $\mathcal{T} = 0.1$ appears to be the optimal value in order to ensure numerical accuracy while minimizing the computational cost.

The effect of $\mathcal{T}$ on the flow in the vicinity of the cylinder is depicted in figures 3(b,c). Both the streamwise flow velocity and shear-rate magnitude remain almost unaltered for $\mathcal{T} \leq 0.1$. In this range, the flow patterns are consistent with the expected creeping flow features. In particular, the flow presents symmetries along both the streamwise and cross-flow directions. The highest shear regions are found close to the edges of the cylinder. In contrast, important flow variations occur for $\mathcal{T} > 0.1$ due to the emergence of compressibility effects. A high shear region emerges downstream of the body and the flow symmetry is broken. Overall, the evolution of the flow pattern is consistent with the rapid variation of the drag coefficient observed in figure 3(a) for $\mathcal{T} > 0.1$.

Details on the numerical setups associated with the data plotted in figure 3 are provided in table 1. It can be noted that the Mach number, Knudsen number and *viscous* relaxation time increase as functions of $\mathcal{T}$. It should be recalled that Kn designates the von Kármán Knudsen number, namely $Kn = Ma/Re$. The value of Kn varies over a wide range and it typically violates the condition $Kn \ll 1$. Moreover, the *viscous* relaxation time greatly

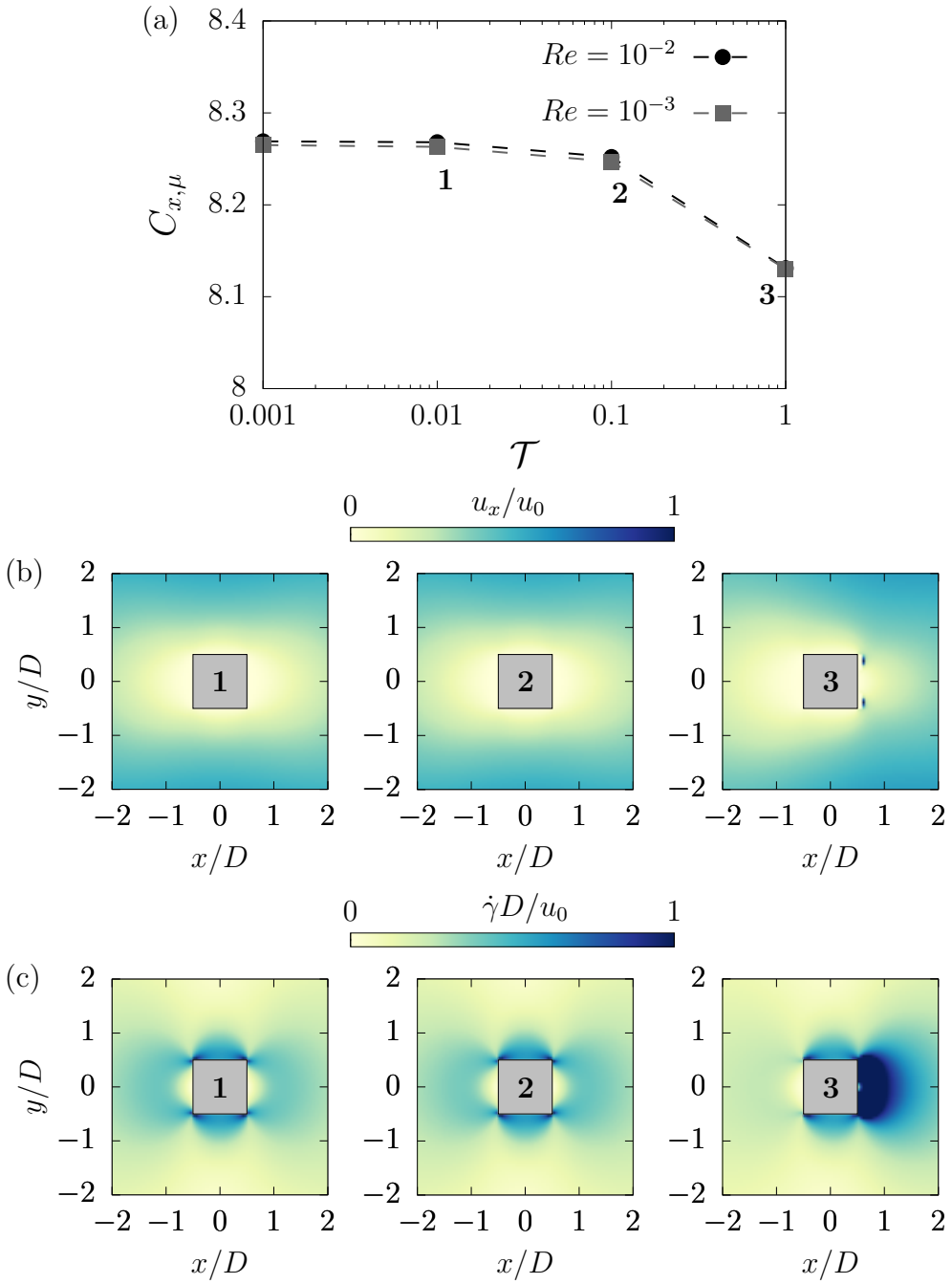

Figure 3: Effect of the incompressibility factor on Newtonian creeping flow simulations: (a) evolution of the drag force coefficient as a function of $\mathcal{T}$, for two values of the Reynolds number $Re \ll 1$, and iso-contours of the non-dimensional (b) streamwise flow velocity and (c) shear-rate magnitude close to the cylinder, for $Re = 10^{-2}$ and for three values of $\mathcal{T}$ indicated by the labels in (a).

		$\mathcal{T}$	Ma	Kn	$\hat{\tau}^+$	$C_{x,\mu}$
Fig. 3	$Re = 10^{-2}$	10^{-3}	3.16×10^{-3}	3.16×10^{-1}	12	8.27
		10^{-2}	10^{-2}	1	36.9	8.27
		10^{-1}	3.16×10^{-2}	3.16	115.4	8.25
		1	10^{-1}	10	364.2	8.13
	$Re = 10^{-3}$	10^{-3}	10^{-3}	1	36.9	8.26
		10^{-2}	3.16×10^{-3}	3.16	115.4	8.26
		10^{-1}	10^{-2}	10	364.2	8.25
		1	3.16×10^{-2}	31.6	1149.9	8.13
Fig. 4	$Re = 10^{-4}$	0.1	3.16×10^{-3}	31.6	1149	8.25
	$Re = 10^{-5}$	0.1	10^{-3}	100	3638	8.25
	$Re = 10^{-6}$	0.1	3.16×10^{-4}	316	11494	8.25

Table 1: Details on the numerical setups analyzed in figures 3 and 4.

departs from unity. In particular, the case $Re = 10^{-3}$ and $\mathcal{T} = 10^{-1}$ shows that accurate simulations can be performed up to $Kn = 10$ and $\hat{\tau}^+ \approx 360$.

To further illustrate that the simulation is not altered by the numerical parameters if the incompressibility factor is fixed, the flow past a square cylinder has been computed over a range of Reynolds numbers $Re \ll 1$ for $\mathcal{T} = 0.1$. The resulting evolution of the drag force coefficient is plotted in figure 4(a). As the Reynolds number decreases, the flow solution approaches the asymptotic creeping flow regime and the drag coefficient $C_{x,\mu}$ rapidly converges to a constant value equal to 8.25, approximately. This limit value is close to the drag value of 8.4 obtained using a linear lattice-Boltzmann model, i.e. by keeping only the first two terms of the equilibrium functions in equation (8), to model the Stokes regime. The viscosity-independence of the drag force in the Stokes regime using the TRT model has been investigated in prior works [9, 10, 13]. Here, the constant evolution of the drag in the range $Re \ll 1$ indicates that the non-linear simulations remain accurate even at very low Reynolds numbers. Other flow quantities also remain unaltered by variations of the Reynolds number in the region $Re \ll 1$. This is depicted in figures 4(b,c), which show the evolutions of the streamwise flow velocity and shear rate along the cross-flow direction for $Re = 10^{-3}$ and $Re = 10^{-5}$, in the vicinity of the body for $x/D = 0$. It can be noted that both simulations result in identical flow solutions. The numerical setups corresponding to the data plotted in figure 4 have also been reported in table 1. Knudsen numbers up to

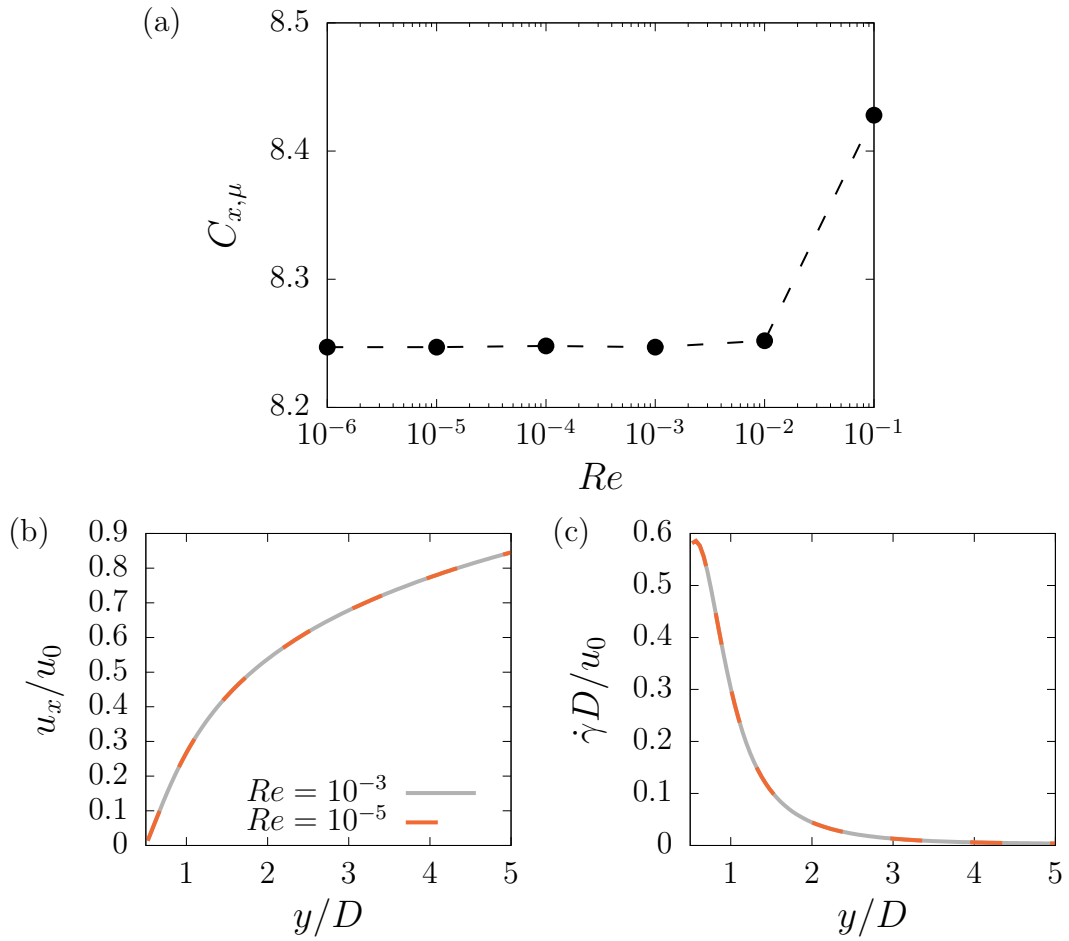

Figure 4: Effect of the Reynolds number $Re \ll 1$ on Newtonian creeping flow simulations, for a fixed incompressibility factor $\mathcal{T} = 0.1$: (a) evolution of the drag force coefficient $C_{x,\mu}$ as a function of Re, and cross-flow evolution of the non-dimensional (b) streamwise velocity and (c) shear-rate magnitude close to the upper square surface at $x/D = 0$, for two values of the Reynolds number.

$Kn \approx 310$ and relaxation times up to $\hat{\tau}^+ \approx 11000$ can be achieved without altering the simulation accuracy, which further supports the theoretical analysis proposed in §3.

5.3. Creeping yield-stress flow past a square cylinder

According to the previous numerical analysis of the Newtonian flow past a square cylinder, the fluid viscosity can be freely varied in the present numerical framework as long as the condition $\mathcal{T} \leq 0.1$ is satisfied. In the following, the focus is placed on yield-stress flow simulations. In this case, large variations of the local incompressibility factor $\mathcal{T}_l$ (39) are expected due to local variations of the flow viscosity. In particular, $\mathcal{T}_l$ may locally exceed the nominal incompressibility factor $\mathcal{T}$ based on the reference viscosity. As described in §4.3, the numerical accuracy is thus ensured by setting the maximum value of $\mathcal{T}_l$ in the simulations. Based on the previous Newtonian analysis, this value is chosen as $\mathcal{T}_{max} = 0.1$. $\mathcal{T}_{max}$ controls the local value of the maximum fluid viscosity, possibly resulting in the trun-

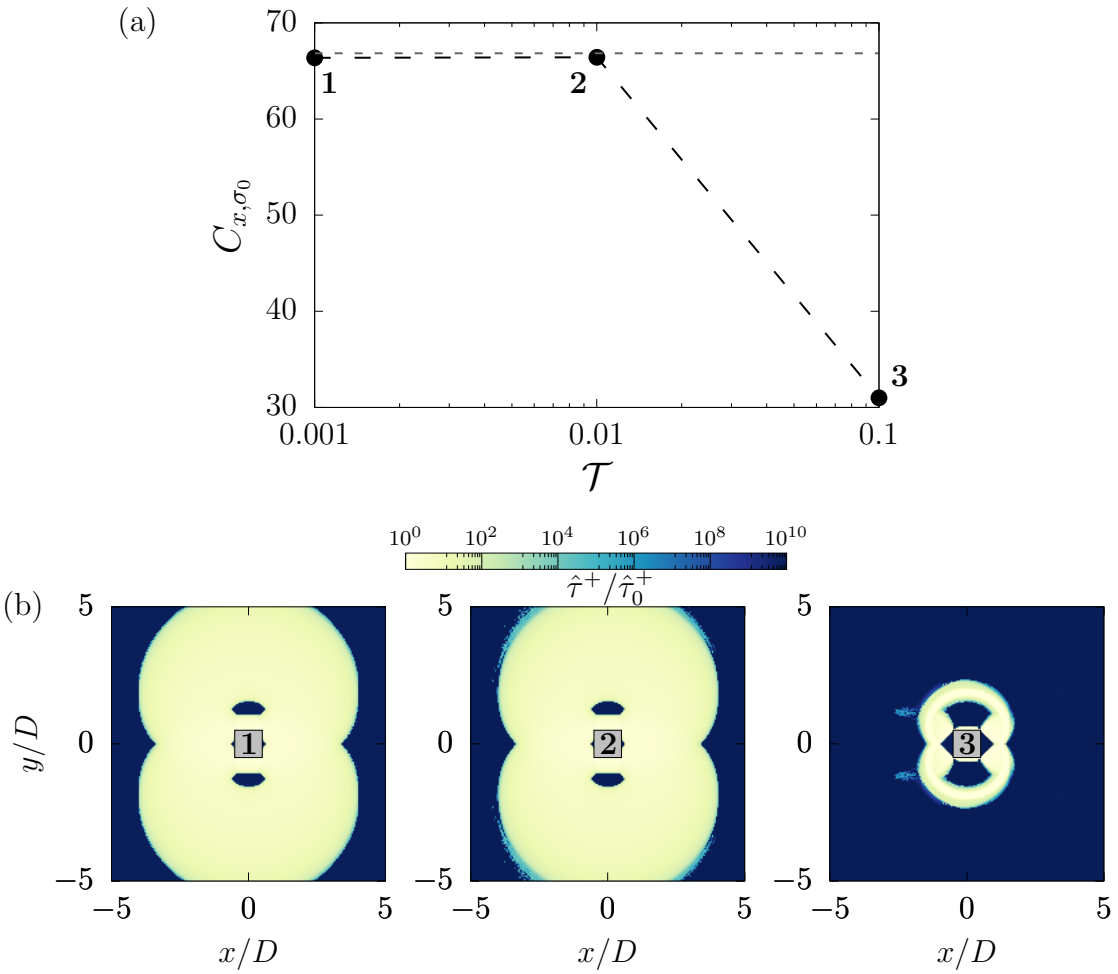

Figure 5: Effect of the global incompressibility parameter $\mathcal{T} = Ma^2/Re$ on yield-stress flow simulations, for $Re = 0.01$ and $Bn = 1$: (a) evolution of the yield drag coefficient C_{x,σ_0} as a function of $\mathcal{T}$, and (b) iso-contours of the normalized viscous relaxation time for three values of $\mathcal{T}$, indicated by the labels reported in (a). Note that the maximal local incompressibility factor $\mathcal{T}_{max}$ is set to 0.1 (see §4.3). In (a), the horizontal dashed line indicates the drag value reported by Nirmalkar et al. [40].

cation of the Herschel-Bulkley law. The nominal incompressibility factor remains a free parameter, that should be chosen in the range $\mathcal{T} \in]0, \mathcal{T}_{max}]$. Small values of $\mathcal{T}$ are expected to allow large viscosity variations. In contrast, viscosity truncation is expected to occur if $\mathcal{T}$ is too close to $\mathcal{T}_{max}$. In practice, the value of $\mathcal{T}_l$ is controlled at each time step. In the present implementation, warning messages are sent to the simulation output when viscosity truncation occurs on one or more lattice nodes. Truncated simulations should be carefully considered: while small and localized viscosity truncations may have negligible effects on the overall flow solution, important truncations can significantly alter the flow accuracy, as illustrated hereafter. Therefore, it is generally recommended to avoid viscosity truncation (by decreasing $\mathcal{T}$) in order to ensure the numerical accuracy.

The effect of $\mathcal{T}$ is examined in the following in the case $Bn = 1$ and $Re = 0.01$. Figure

5(a) shows the evolution of the drag force coefficient over the range $\mathcal{T} \in [0.001, 0.1]$. The drag force exhibits a constant evolution for $\mathcal{T} \leq 0.01$. In this region, no viscosity truncation occurs, i.e. the Herschel-Bulkley law is fully recovered in the limit of the floating point approximation (see §4.1). In addition, the predicted value of the drag is in agreement with the force computed by Nirmalkar et al. [40], which has been reported in the figure. As expected, the case $\mathcal{T} = \mathcal{T}_{max} = 0.1$ results in viscosity truncation. The effect of the truncation on the drag force is clearly noted in figure 5(a).

The viscosity patterns associated with the three simulations reported in figure 5(a) are depicted in figure 5(b) using iso-contours of the local *viscous* relaxation time. As expected from figure 5(a), similar patterns are observed for $\mathcal{T} = 0.001$ and $\mathcal{T} = 0.01$. The flow exhibits sharp interfaces between *solid*- and *fluid*-like regions, called yield surfaces [40]. These interfaces are associated with considerable viscosity ratios, extending over more than 10 orders of magnitude. In particular, substantially large viscosities appear in low-shear regions, as allowed by the present definition of μ_{max}. The viscosity pattern is in agreement with previously reported simulation results [40]. The *fluid* region exhibits a figure-eight shape in the vicinity of the body. Three types of *solid* regions are observed: (i) the far-field region, where the fluid follows a *solid* motion, (ii) two isolated regions of *solid* rotation on the upper and lower sides of the body, and (iii) two triangular stagnation regions attached to the upstream and downstream sides of the cylinder. A major alteration of the flow is noted when the Herschel-Bulkley law is truncated, as illustrated by the case $\mathcal{T} = 0.1$.

The described flow pattern has implications on the effect of the domain size on the flow solution. Indeed, the emergence of a *solid*-like region away from the body indicates that the flow is close to uniform in these regions. If the computational boundaries are far enough from the body surface to allow this *fluid*/*solid* transition, their effect on the flow is thus expected to be limited, even though the Reynolds number is small. This is confirmed by the domain size convergence study performed by Nirmalkar et al. [40].

The evolution of the drag force as a function of the Bingham number is examined in figure 6(a). The maximum incompressibility factor is maintained to $\mathcal{T}_{max} = 0.1$. As Bn increases, the global incompressibility factor has to be decreased in order to avoid viscosity truncation. The values $\mathcal{T} = 10^{-2},\ 10^{-3},\ 10^{-4},\ 10^{-5}$ have been employed for the cases $Bn = 1,\ 10,\ 100,\ 1000$, respectively. Note that the relevant value of $\mathcal{T}$ can be estimated *a priori*, thus avoiding unnecessary numerical tests. Indeed, the typical value of $\mathcal{T}_l$ can be expressed, using $\dot{\gamma} \approx u_0/D$, as $\mathcal{T}_l = T(1 + Bn)$. The condition $\mathcal{T}_l < \mathcal{T}_{max}$ thus leads to $\mathcal{T} < \mathcal{T}_{max}/(1 + Bn)$, indicating that in the range $Bn \gg 1$, $\mathcal{T}$ should be divided by 10 when Bn is multiplied by 10. The data issued from the numerical work of Nirmalkar et al. [40] have been reported in figure 6(a) for comparison purpose. An excellent agreement is noted between both studies.

The *solid* and *fluid* regions are determined by defining the yield surface as the iso-contour $\dot{\gamma} = \epsilon$, with $\epsilon \ll 1$. The value $\epsilon = 10^{-3}$ is used in the following. The resulting patterns are plotted in figure 6(b) for three values of the Bingham number. The evolution of the yield surface is well-captured by the present simulations, and the predicted patterns are consistent with the numerical results of Nirmalkar et al. [40]. Overall, the size of the *fluid* region tends to decrease as a function of Bn. In contrast, *solid* regions are extended, leading

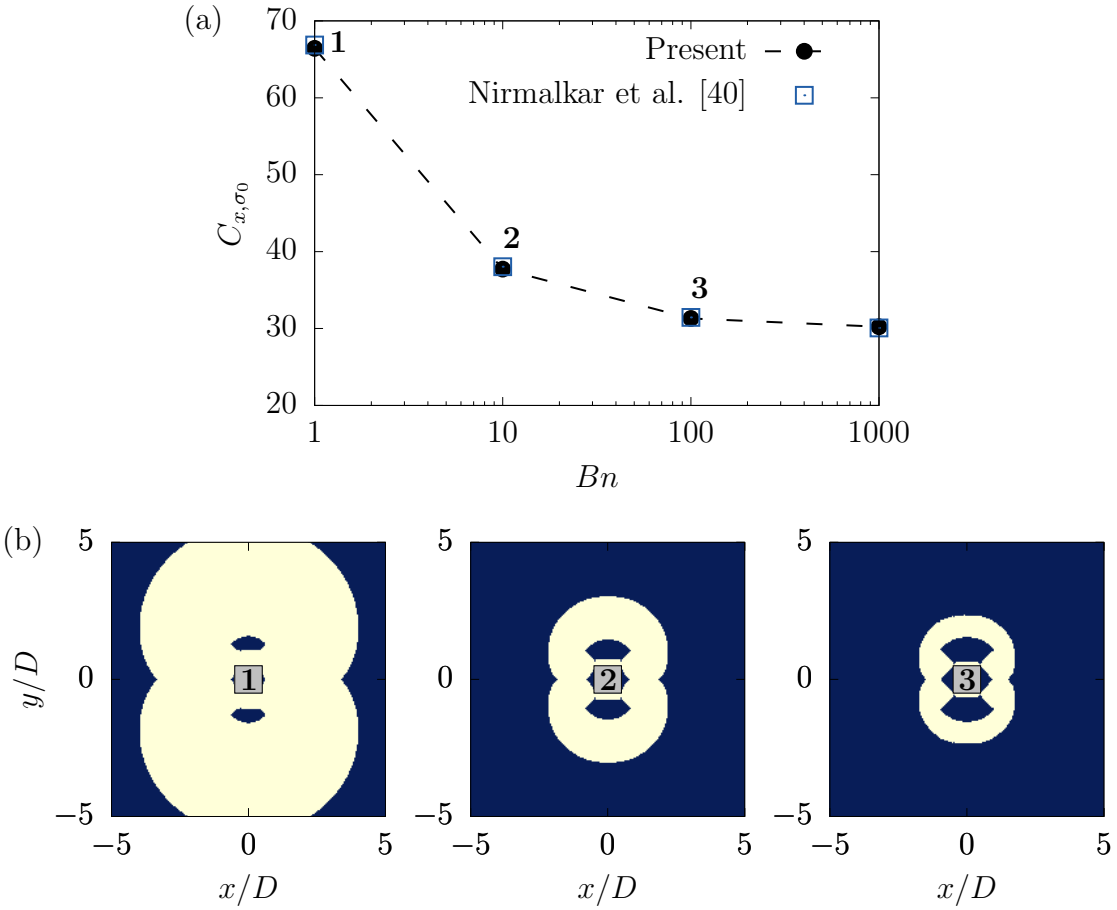

Figure 6: Effect of the Bingham number Bn on yield-stress flow simulations, for $Re = 0.01$: (a) evolution of the yield drag coefficient C_{x,σ_0} as a function of Bn, predicted by the present simulations and reported by Nirmalkar et al. [40], and (b) visualization of the yield surface for three values of Bn, indicated by the labels reported in (a).

to the formation of two equilateral triangular stagnation regions and two large *solid*-rotation regions at large Bingham numbers.

5.4. Creeping shear-thinning and shear-thickening flows past a square cylinder

Simulations of shear-thinning and shear-thickening flows are considered in the following. The Bingham number is set to zero, and the simulations are performed over a range of the flow index n for $Re = 0.01$. Following the same procedure as that employed in the previous section, the maximum incompressibility parameter $\mathcal{T}_{max}$ is set to 0.1. All simulations are performed with $\mathcal{T} = 0.01$, a value that is small enough to avoid any viscosity cut-off over the range $n \in [0.2, 1.8]$.

The evolution of the drag force coefficient is plotted in figure 7(a). The drag force significantly decreases as a function of the flow index. The numerical data of Pantokratoras [39] have also been reported in the figure. These data correspond to the unconfined simulations

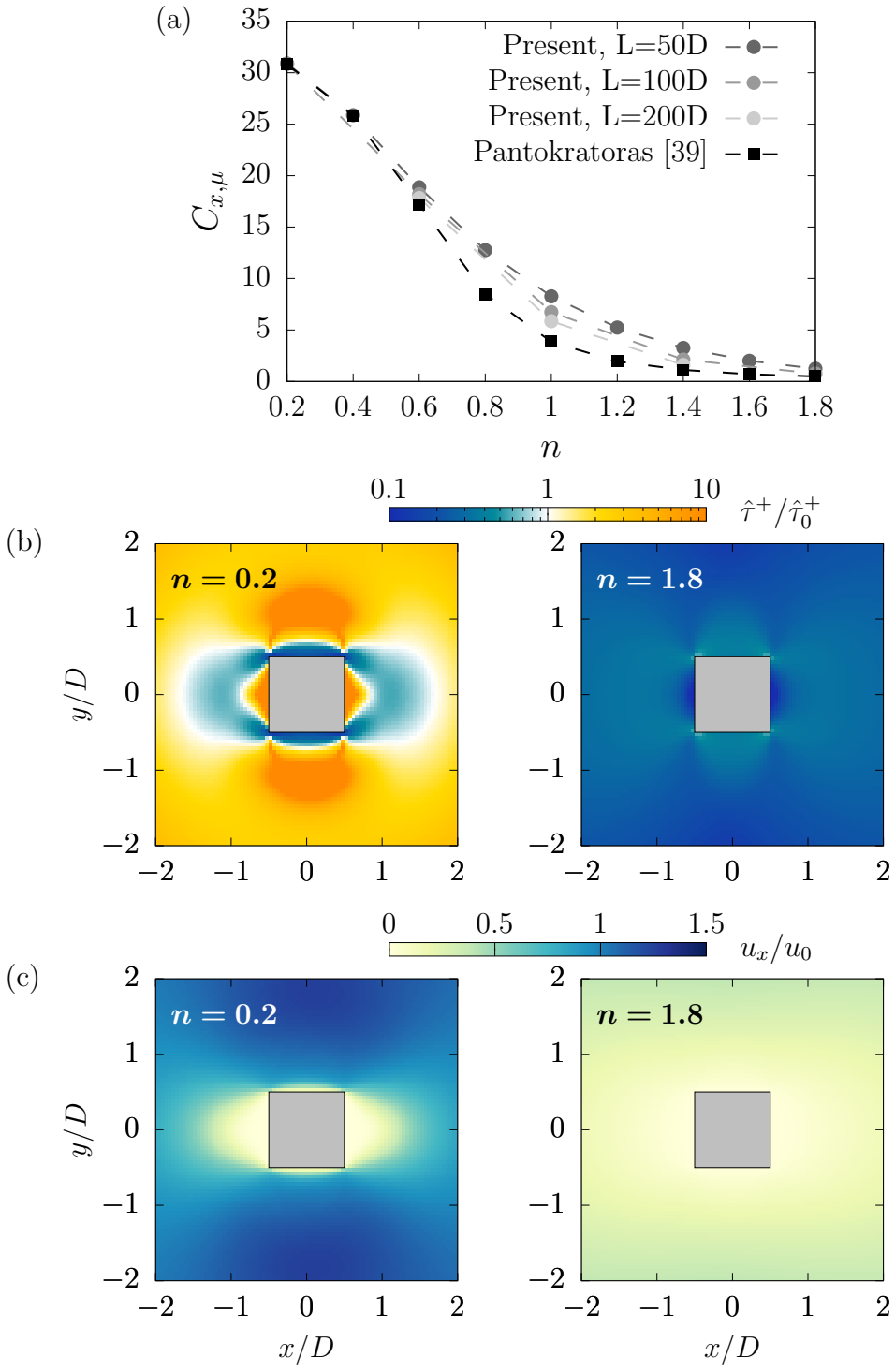

Figure 7: Effect of the flow index n of shear-thinning and shear-thickening simulations: (a) evolution of the drag coefficient as a function of n, for different computational domain sizes L and compared to the unconfined numerical results reported by Pantokratoras [39], and iso-contours of (b) the normalized relaxation time and (c) the non-dimensional streamwise flow velocity in the vicinity of the body in the case $L = 100D$, for $n = 0.2$ and $n = 1.8$.

performed in that study, carried out with a domain size $L = 50000D$. A good agreement is observed between both studies in highly shear-thinning and highly shear-thickening regions. However, the drag force predicted by the present simulations is substantially higher when the flow index in close to one. These deviations are expected to relate to blockage effects, as Pantokratoras [39] pointed out that very large computational domains must be used in this case to achieve unconfined simulations. Additional computations with larger domains have been performed in order to examine this aspect. These simulations, also reported in figure 7(a), confirm that the present drag force tends to the one computed by Pantokratoras [39] as the domain size increases. The effect of the domain size is however contrasted over the range of flow indices, as important variations of the drag force are principally observed when n is close to 1.

Figures 7(b,c) present visualizations of the flow in the vicinity of the cylinder for two values of the flow index, namely $n = 0.2$ and $n = 1.8$, corresponding to highly shear-thinning and highly shear-thickening cases. Figure 7(b) shows iso-contours of the *viscous* relaxation time. Overall, it can be noted that variations of the flow viscosity are much less pronounced than in the case of the yield-stress flow, visualized in figure 5. Shear-thinning and shear-thickening simulations can thus be considered to be less critical regarding the effect of the fluid viscosity on the numerical accuracy. It should be noted that when $n = 0.2$, the flow tends to exhibit large viscosities in low-shear regions, i.e. the shear-thinning property does not systematically result in a viscosity decrease compared to the reference viscosity. These low-shear regions are encountered in the far-field region, but also close to the body near the upstream and downstream square surfaces. Similarly, low-viscosity regions emerge in the shear-thickening case. In both cases, viscosity variations are mostly found close to the body surface. The shear-thinning case however exhibits larger viscosity gradients; in particular, thin low-viscosity layers are noted on the upper and lower body surfaces. These smaller flow length scales can be clearly noted in figure 7(c), which shows iso-contours of the streamwise flow velocity. The important viscosity decrease close to the cylinder surface in the shear-thinning case results in remarkably thin boundary layers. Similar behaviors, especially characterized by a major increase of the wall vorticity when the flow index n decreases, have been observed in prior simulations of shear-thinning flows past bluff bodies [41]. Consequently, the far-field flow velocity is rapidly recovered away from the body. This is consistent with the small blockage effects observed in the low-n region in figure 7(a). In contrast, the shear-thickening flow exhibits much smoother velocity variations, which might increase the effect of the domain size in this case. The important effect of n on the flow length scale is further illustrated in figure 8, which shows far-field iso-contours of the non-dimensional streamwise flow velocity for $n = 0.2$ and $n = 1.8$. This evolution has important numerical implications, as either large computational domains or fine mesh resolutions may be required to achieve high numerical accuracy, depending on the value of the flow index.

6. Summary

This paper provides general guidelines for the simulation of highly viscous steady flows based on a general two-relaxation-time lattice-Boltzmann framework. The analysis of the

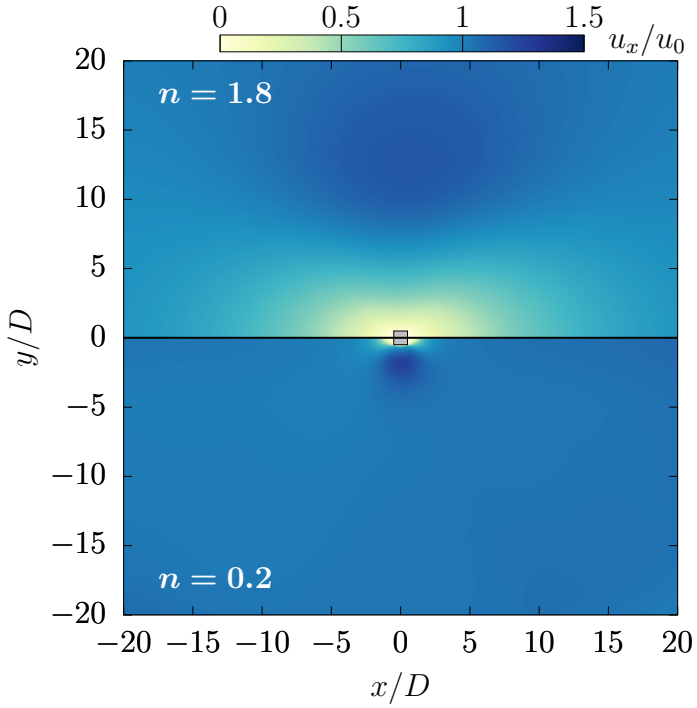

Figure 8: Effect of n on the flow length scale at $Re = 0.01$: far-field iso-contours of the non-dimensional streamwise flow velocity for (bottom) $n = 0.2$ and (top) $n = 1.8$. The size of the computational domain is $L = 100D$.

space-continuous mesoscopic equations, performed through Hermite projection and multi-scale expansion, shows that hydrodynamic behavior can be recovered at the macroscopic scale for any fluid viscosity, provided that the product of both relaxation times $\tau^+\tau^-$ remains small enough. An alternative definition of the Knudsen number, controlling the magnitude of the non-equilibrium part of the mesoscopic solution, must however be considered, namely $Kn^* = \sqrt{\tau^+\tau^-}c_s/D$. Its magnitude can be controlled by varying τ^- which is a free numerical parameter. The present analysis supports previous works showing that bulk numerical solutions of the discrete TRT lattice-Boltzmann equation are viscosity-independent if $\Lambda = \tau^+\tau^-$, which controls the magnitude of numerical errors, is kept constant [17].

The main limitation concerning the fluid viscosity emerges when deriving the non-dimensional macroscopic equations, which involves viscosity-dependent compressibility terms. In order to achieve incompressibility, the incompressibility parameter $\mathcal{T} = Ma^2/Re$ must satisfy $\mathcal{T} \ll 1$. A local definition of $\mathcal{T}$ is proposed to control the accuracy of the flow in simulations involving variable viscosities, i.e. non-Newtonian fluids. This analysis shows that considerably large fluid viscosities can be numerically allowed in low-shear regions, a feature that proved to be useful for yield-stress flow simulations.

These properties have been confirmed based on a series of numerical simulations of the creeping flow past a square cylinder. When the fluid is Newtonian, incompressibility of the flow is ensured for $\mathcal{T} = 0.1$. This value of $\mathcal{T}$ should be used in future works to set the value of the Mach number in low-Reynolds-number simulations and to minimize the computational cost. Once $\mathcal{T}$ and Kn^* are fixed, highly viscous simulations can be performed: relaxation

times up to 10^4 are employed in the present work without any effect on the flow solution.

Non-Newtonian flows have been simulated using an Herschel-Bulkley fluid model. If the local value of $\mathcal{T}$ is properly controlled, major viscosity variations can be reproduced. Yield-stress flow solutions exhibit sharp yield-surfaces associated with viscosity ratios larger than 10^{10}. Simulations have been performed over the range of Bingham numbers $Bn \in [1, 1000]$, i.e. including regimes that had not been simulated using the LB method; the predicted flow solutions are in agreement with previous numerical results based on Navier-Stokes methods. Shear-thinning and shear-thickening flows are also accurately reproduced over a wide range of flow indices $n \in [0.2, 1.8]$.

Acknowledgements

We thank Song Zhao for useful discussions. The project MACBION leading to this publication has received funding from Excellence Initiative of Aix-Marseille University - A*MIDEX, a French Investissements d'Avenir programme and the SINUMER project (ANR-18-CE45-0009-01) of the French National Research Agency (ANR).

Appendix A. Symmetric and anti-symmetric population properties

Equilibrium and non-equilibrium populations are decomposed into symmetric and anti-symmetric parts,

$$f_i^{eq+} = \frac{1}{2}(f_i^{eq} + f_{\bar{i}}^{eq}) \; ; \; f_i^{eq-} = \frac{1}{2}(f_i^{eq} - f_{\bar{i}}^{eq}), \tag{A.1}$$

and

$$f_i^{neq+} = \frac{1}{2}(f_i^{neq} + f_{\bar{i}}^{neq}) \; ; \; f_i^{neq-} = \frac{1}{2}(f_i^{neq} - f_{\bar{i}}^{neq}), \tag{A.2}$$

satisfying $f_i^{eq} = f_i^{eq+} + f_i^{eq-}$ and $f_i^{neq} = f_i^{neq+} + f_i^{neq-}$. It should be recalled that the following identities are also satisfied by these functions:

$$\sum_i f_i^{eq} = \sum_i f_i = \rho \;\; ; \;\; \sum_i f_i^{eq} \boldsymbol{c_i} = \sum_i f_i \boldsymbol{c_i} = \rho \boldsymbol{u} \tag{A.3}$$

and

$$\sum_i f_i^{neq} = 0 \;\; ; \;\; \sum_i f_i^{neq} \boldsymbol{c_i} = 0. \tag{A.4}$$

Furthermore, moments of f_i are fully recovered by the symmetric populations at even orders and by the anti-symmetric ones at odd orders. At orders 0 and 1, this is expressed as

$$\sum_i f_i^{eq+} = \rho \;\; ; \;\; \sum_i f_i^{eq-} = 0 \;\; ; \;\; \sum_i f_i^{neq+} = \sum_i f_i^{neq-} = 0, \tag{A.5}$$

and

$$\sum_i f_i^{eq+} \boldsymbol{c_i} = 0 \;\; ; \;\; \sum_i f_i^{eq-} \boldsymbol{c_i} = \rho \boldsymbol{u} \;\; ; \;\; \sum_i f_i^{neq+} \boldsymbol{c_i} = \sum_i f_i^{neq-} \boldsymbol{c_i} = 0. \tag{A.6}$$

More generally, this property may be expressed for any n-order moment $\boldsymbol{P}^{(n)} = \sum_i f_i \boldsymbol{c_i}^n$ as

$$\boldsymbol{P}^{(n)} = \boldsymbol{P}^{(n)+} = \sum_i f_i^+ \boldsymbol{c_i}^n \qquad \text{if n is even} \tag{A.7}$$

and

$$\boldsymbol{P}^{(n)} = \boldsymbol{P}^{(n)-} = \sum_i f_i^- \boldsymbol{c_i}^n \qquad \text{if n is odd.} \tag{A.8}$$

Appendix B. Second-order Hermite projection of the TRT Boltzmann equation

The second-order projection of the TRT Boltzmann equation reads

$$\frac{\partial}{\partial x_\alpha}(\mathcal{Q}_{\alpha\beta\gamma} - \rho c_s^2 u_\alpha \delta_{\beta\gamma}) = -\frac{1}{\tau^+}\Pi_{\beta\gamma}^{neq+} - \frac{1}{\tau^-}\Pi_{\beta\gamma}^{neq-}, \tag{B.1}$$

where $\mathcal{Q}_{\alpha\beta\gamma}$ is the third-order moment defined by $\mathcal{Q}_{\alpha\beta\gamma} = \sum_i f_i c_{i,\alpha} c_{i,\beta} c_{i,\gamma}$ and $\Pi_{\beta\gamma}^{neq+}$ and $\Pi_{\beta\gamma}^{neq-}$ are the symmetric and anti-symmetric parts of $\Pi_{\beta\gamma}^{neq}$. It can be shown that, due to symmetry ($c_{i,\beta}c_{i,\gamma} = c_{\bar{i},\beta}c_{\bar{i},\gamma}$), $\Pi_{\beta\gamma}^{neq-} = 0$ and $\Pi_{\beta\gamma}^{neq+} = \Pi_{\beta\gamma}^{neq}$:

$$\Pi_{\beta\gamma}^{neq-} = \frac{1}{2}\sum_i f_i^{neq} c_{i,\beta}c_{i,\gamma} - \frac{1}{2}\sum_i f_{\bar{i}}^{neq} c_{i,\beta}c_{i,\gamma} = 0, \tag{B.2a}$$

$$\Pi_{\beta\gamma}^{neq+} = \frac{1}{2}\sum_i f_i^{neq} c_{i,\beta}c_{i,\gamma} + \frac{1}{2}\sum_i f_{\bar{i}}^{neq} c_{i,\beta}c_{i,\gamma} = \Pi_{\beta\gamma}^{neq}. \tag{B.2b}$$

The equilibrium part of $\mathcal{Q}_{\alpha\beta\gamma}$ can be computed using the equilibrium distributions, namely $\mathcal{Q}_{\alpha\beta\gamma}^{eq} = \rho u_\alpha u_\beta u_\gamma + \rho c_s^2(u_\alpha\delta_{\beta\gamma} + u_\beta\delta_{\alpha\gamma} + u_\gamma\delta_{\alpha\beta})$. Equation (B.1) thus becomes

$$\frac{\partial}{\partial x_\alpha}(\rho u_\alpha u_\beta u_\gamma + \rho c_s^2(u_\beta\delta_{\alpha\gamma} + u_\gamma\delta_{\alpha\beta}) + \mathcal{Q}_{\alpha\beta\gamma}^{neq}) = -\frac{1}{\tau^+}\Pi_{\beta\gamma}^{neq}. \tag{B.3}$$

This second-order projection is then simplified by linear combination with the first-order equation (16). Multiplying (16) by u_γ gives

$$\frac{\partial}{\partial x_\alpha}(\rho u_\alpha u_\beta u_\gamma) - \rho u_\alpha u_\beta \frac{\partial}{\partial x_\alpha}(u_\gamma) + u_\gamma \frac{\partial}{\partial x_\beta}(\rho c_s^2) + u_\gamma \frac{\partial}{\partial x_\alpha}(\Pi_{\alpha\beta}^{neq}) = 0. \tag{B.4}$$

A similar expression can be obtained by expressing (16) on indices α and γ and multiplying it by u_β, namely

$$\frac{\partial}{\partial x_\alpha}(\rho u_\alpha u_\beta u_\gamma) - \rho u_\alpha u_\gamma \frac{\partial}{\partial x_\alpha}(u_\beta) + u_\beta \frac{\partial}{\partial x_\gamma}(\rho c_s^2) + u_\beta \frac{\partial}{\partial x_\alpha}(\Pi_{\alpha\gamma}^{neq}) = 0. \tag{B.5}$$

Subtracting (B.4) and (B.5) to (B.3), a new second-order projection is obtained:

$$\begin{aligned} &-\frac{\partial}{\partial x_\alpha}(\rho u_\alpha u_\beta u_\gamma) + \rho u_\alpha \frac{\partial}{\partial x_\alpha}(u_\beta u_\gamma) + \rho c_s^2\left(\frac{\partial u_\gamma}{\partial x_\beta} + \frac{\partial u_\beta}{\partial x_\gamma}\right) \\ &+ \frac{\partial}{\partial x_\alpha}(\mathcal{Q}_{\alpha\beta\gamma}^{neq}) - u_\gamma \frac{\partial}{\partial x_\alpha}(\Pi_{\alpha\beta}^{neq}) - u_\beta \frac{\partial}{\partial x_\alpha}(\Pi_{\alpha\gamma}^{neq}) = \frac{-\Pi_{\beta\gamma}^{neq}}{\tau^+}. \end{aligned} \tag{B.6}$$

Noticing that $\rho u_\alpha \dfrac{\partial}{\partial x_\alpha}(u_\beta u_\gamma) = \dfrac{\partial}{\partial x_\alpha}(\rho u_\alpha u_\beta u_\gamma)$ due to the mass conservation equation (14), and defining the shear-rate tensor $S_{\alpha\beta} = \dfrac{1}{2}(\dfrac{\partial u_\alpha}{\partial x_\beta} + \dfrac{\partial u_\beta}{\partial x_\alpha})$, equation (B.6) simplifies to

$$2\rho c_s^2 S_{\beta\gamma} + \frac{\partial}{\partial x_\alpha}(\mathcal{Q}^{neq}_{\alpha\beta\gamma}) - u_\gamma \frac{\partial}{\partial x_\alpha}(\Pi^{neq}_{\alpha\beta}) - u_\beta \frac{\partial}{\partial x_\alpha}(\Pi^{neq}_{\alpha\gamma}) = \frac{-\Pi^{neq}_{\beta\gamma}}{\tau^+}. \tag{B.7}$$

Appendix C. Equilibrium solutions of the TRT Boltzmann equation

First, the dynamic equation for the symmetric populations f_i^+ is derived using

$$\frac{\partial}{\partial x_\alpha}\left(c_{i\alpha} f_i^+\right) = \frac{1}{2}\frac{\partial}{\partial x_\alpha}\left(c_{i\alpha} f_i\right) - \frac{1}{2}\frac{\partial}{\partial x_\alpha}\left(c_{\bar{i}\alpha} f_{\bar{i}}\right), \tag{C.1}$$

which can be rewritten as a function of the collision operators using equation (11),

$$\frac{\partial}{\partial x_\alpha}\left(c_{i\alpha} f_i^+\right) = -\frac{1}{2\tau^+} f_i^{neq+} - \frac{1}{2\tau^-} f_i^{neq-} + \frac{1}{2\tau^+} f_{\bar{i}}^{neq+} + \frac{1}{2\tau^-} f_{\bar{i}}^{neq-}. \tag{C.2}$$

Noticing that $f_{\bar{i}}^+ = f_i^+$ and $f_{\bar{i}}^- = -f_i^-$, this equation becomes

$$\frac{\partial}{\partial x_\alpha}\left(c_{i\alpha} f_i^+\right) = -\frac{1}{\tau^-} f_i^{neq-}. \tag{C.3}$$

Similarly, it can be shown that the dynamics of the antisymmetric populations is governed by

$$\frac{\partial}{\partial x_\alpha}\left(c_{i\alpha} f_i^-\right) = -\frac{1}{\tau^+} f_i^{neq+}. \tag{C.4}$$

Summing equations (C.3) and (C.4), the non-equilibrium functions satisfy

$$-f_i^{neq} = \tau^- \frac{\partial}{\partial x_\alpha}\left(c_{i\alpha} f_i^+\right) + \tau^+ \frac{\partial}{\partial x_\alpha}\left(c_{i\alpha} f_i^-\right). \tag{C.5}$$

Developing f_i^+ as a function of f_i and f_i^-, namely $f_i^+ = f_i - f_i^-$, gives

$$-f_i^{neq} = \tau^- \frac{\partial}{\partial x_\alpha}\left(c_{i\alpha} f_i\right) + (\tau^- - \tau^+)\frac{\partial}{\partial x_\alpha}\left(c_{i\alpha} f_i^+\right). \tag{C.6}$$

A similar equation can be obtained by developing f_i^- as a function of f_i and f_i^+,

$$-f_i^{neq} = \tau^+ \frac{\partial}{\partial x_\alpha}\left(c_{i\alpha} f_i\right) + (\tau^+ - \tau^-)\frac{\partial}{\partial x_\alpha}\left(c_{i\alpha} f_i^-\right). \tag{C.7}$$

Finally, the non-equilibrium distribution functions can be expressed as functions of f_i and $f_{\bar{i}}$ by summing equations (C.6) and (C.7),

$$-2f_i^{neq} = (\tau^+ + \tau^-)\frac{\partial}{\partial x_\alpha}\left(c_{i\alpha} f_i\right) - (\tau^+ - \tau^-)\frac{\partial}{\partial x_\alpha}\left(c_{i\alpha} f_{\bar{i}}\right). \tag{C.8}$$

On the other hand, non-equilibrium populations $f_{\bar{i}}^{neq}$ also satisfy

$$-2f_{\bar{i}}^{neq} = (\tau^+ - \tau^-)\frac{\partial}{\partial x_\alpha}(c_{i\alpha}f_i) - (\tau^+ + \tau^-)\frac{\partial}{\partial x_\alpha}(c_{i\alpha}f_{\bar{i}})\,. \tag{C.9}$$

When the non-equilibrium functions vanish, namely $f_i^{neq} = f_{\bar{i}}^{neq} = 0$, equations (C.8) and (C.9) lead to

$$\frac{\partial}{\partial x_\alpha}(c_{i\alpha}f_i) = \frac{\tau^+ - \tau^-}{\tau^+ + \tau^-}\frac{\partial}{\partial x_\alpha}(c_{i\alpha}f_{\bar{i}})\,, \tag{C.10a}$$

$$\frac{\partial}{\partial x_\alpha}(c_{i\alpha}f_i) = \frac{\tau^+ + \tau^-}{\tau^+ - \tau^-}\frac{\partial}{\partial x_\alpha}(c_{i\alpha}f_{\bar{i}})\,, \tag{C.10b}$$

which is equivalent to

$$\frac{\tau^+ - \tau^-}{\tau^+ + \tau^-} = \frac{\tau^+ + \tau^-}{\tau^+ - \tau^-} \Longleftrightarrow \tau^+\tau^- = 0. \tag{C.11}$$

References

[1] Z. Guo, C. Shu, Lattice Boltzmann method and its applications in engineering, Advances in computational fluid dynamics, World Scientfic, 2013.

[2] T. Krüger, H. Kusumaatmaja, A. Kuzmin, O. Shardt, G. Silva, E. M. Viggen, The Lattice Boltzmann Method: Principles and Practice, Springer International Publishing, 2017.

[3] U. Frisch, D. d'Humieres, B. Hasslacher, P. Lallemand, Y. Pomeau, J.-P. Rivet, Lattice gas hydrodynamics in two and three dimensions, Complex Systems 1 (4) (1987) 649–707.

[4] F. Higuera, S. Succi, R. Benzi, Lattice gas dynamics with enhanced collisions, EPL (Europhysics Letters) 9 (4) (1989) 345.

[5] S. Chen, G. D. Doolen, Lattice Boltzmann method for fluid flows, Annual Review of Fluid Mechanics 30 (1) (1998) 329364.

[6] X. Shan, X.-F. Yuan, H. Chen, Kinetic theory representation of hydrodynamics: a way beyond the Navier-Stokes equation, Journal of Fluid Mechanics 550 (1) (2006) 413.

[7] S. Chapman, T. G. Cowling, The Mathematical Theory of Non-uniform Gases, 2nd edn., Cambridge University Press, Cambridge, 1952.

[8] G. Karniadakis, A. Beskok, N. Aluru, Microflows and nanoflows: fundamentals and simulation, Vol. 29, Springer Science & Business Media, 2006.

[9] I. Ginzburg, D. d'Humieres, Multireflection boundary conditions for lattice Boltzmann models, Physical Review E 68 (6) (2003) 066614.

[10] L. Talon, D. Bauer, N. Gland, S. Youssef, H. Auradou, I. Ginzburg, Assessment of the two relaxation time Lattice-Boltzmann scheme to simulate Stokes flow in porous media, Water Resources Research 48 (4).

[11] E. Lauga, Continuous breakdown of Purcells scallop theorem with inertia, Physics of Fluids 19 (6) (2007) 061703.

[12] I. Ginzburg, K. Steiner, A free-surface lattice Boltzmann method for modelling the filling of expanding cavities by Bingham fluids, Philosophical Transactions of the Royal Society of London. Series A: Mathematical, Physical and Engineering Sciences 360 (1792) (2002) 453–466.

[13] S. Khirevich, I. Ginzburg, U. Tallarek, Coarse-and fine-grid numerical behavior of MRT/TRT lattice-Boltzmann schemes in regular and random sphere packings, Journal of Computational Physics 281 (2015) 708–742.

[14] P. Lallemand, L.-S. Luo, Theory of the lattice Boltzmann method: Dispersion, dissipation, isotropy, galilean invariance, and stability, Physical Review E 61 (6) (2000) 65466562.
[15] I. Ginzburg, F. Verhaeghe, Two-relaxation-time lattice Boltzmann scheme: About parametrization, velocity, pressure and mixed boundary conditions, Communications in Computanional Physics (2008) 52.
[16] S. Gsell, U. D'Ortona, J. Favier, Explicit and viscosity-independent immersed-boundary scheme for the lattice Boltzmann method, Physical Review E 100 (3) (2019) 033306.
[17] D. d'Humières, I. Ginzburg, Viscosity independent numerical errors for lattice Boltzmann models: From recurrence equations to magic collision numbers, Computers & Mathematics with Applications 58 (5) (2009) 823840.
[18] F. Irgens, Rheology and Non-Newtonian Fluids, Springer International Publishing, 2014.
[19] T. Krüger, F. Varnik, D. Raabe, Shear stress in lattice Boltzmann simulations, Physical Review E 79 (4) (2009) 046704.
[20] S. Gabbanelli, G. Drazer, J. Koplik, Lattice Boltzmann method for non-Newtonian (power-law) fluids, Physical Review E 72 (4) (2005) 046312.
[21] J. Boyd, J. Buick, S. Green, A second-order accurate lattice Boltzmann non-Newtonian flow model, Journal of Physics A: Mathematical and General 39 (46) (2006) 1424114247.
[22] Z. Chai, B. Shi, Z. Guo, F. Rong, Multiple-relaxation-time lattice Boltzmann model for generalized Newtonian fluid flows, Journal of Non-Newtonian Fluid Mechanics 166 (56) (2011) 332342.
[23] D. Conrad, A. Schneider, M. Bhle, Accuracy of non-Newtonian lattice Boltzmann simulations, Journal of Computational Physics 301 (2015) 218229.
[24] L. Talon, D. Bauer, On the determination of a generalized darcy equation for yield-stress fluid in porous media using a Lattice-Boltzmann TRT scheme, The European Physical Journal E 36 (12) (2013) 139.
[25] P. L. Bhatnagar, E. P. Gross, M. Krook, A model for collision processes in gases. I. small amplitude processes in charged and neutral one-component systems, Physical Review 94 (3) (1954) 511525.
[26] I. Ginzburg, D. d'Humières, A. Kuzmin, Optimal stability of advection-diffusion lattice Boltzmann models with two relaxation times for positive/negative equilibrium, Journal of Statistical Physics 139 (6) (2010) 10901143.
[27] A. Kuzmin, I. Ginzburg, A. Mohamad, The role of the kinetic parameter in the stability of two-relaxation-time advection–diffusion lattice boltzmann schemes, Computers & Mathematics with Applications 61 (12) (2011) 3417–3442.
[28] S. Gsell, U. D'Ortona, J. Favier, Multigrid dual-time-stepping lattice Boltzmann method, Physical Review E 101 (2) (2020) 023309.
[29] C. Coreixas, G. Wissocq, G. Puigt, J.-F. Boussuge, P. Sagaut, Recursive regularization step for high-order lattice Boltzmann methods, Physical Review E 96 (3) (2017) 033306.
[30] L. Giraud, D. d'Humieres, P. Lallemand, A lattice Boltzmann model for Jeffreys viscoelastic fluid, EPL (Europhysics Letters) 42 (6) (1998) 625.
[31] I. Lashgari, J. O. Pralits, F. Giannetti, L. Brandt, First instability of the flow of shear-thinning and shear-thickening fluids past a circular cylinder, Journal of Fluid Mechanics 701 (2012) 201227.
[32] S. Mossaz, P. Jay, A. Magnin, Non-recirculating and recirculating inertial flows of a viscoplastic fluid around a cylinder, Journal of Non-Newtonian Fluid Mechanics 177178 (2012) 6475.
[33] S. Farnoush, M. T. Manzari, An investigation on the body force modeling in a lattice Boltzmann BGK simulation of generalized Newtonian fluids, Physica A: Statistical Mechanics and its Applications 415 (2014) 315332.
[34] W. Wu, X. Huang, H. Yuan, F. Xu, J. Ma, A modified lattice Boltzmann method for Herschel-Bulkley fluids, Rheologica Acta 56 (4) (2017) 369376.
[35] T. C. Papanastasiou, Flows of materials with yield, Journal of Rheology 31 (5) (1987) 385404.
[36] S. Mossaz, P. Jay, A. Magnin, Criteria for the appearance of recirculating and non-stationary regimes behind a cylinder in a viscoplastic fluid, Journal of Non-Newtonian Fluid Mechanics (2122) (2010) 1525–1535.
[37] Q. Zou, X. He, On pressure and velocity boundary conditions for the lattice Boltzmann BGK model,

Physics of fluids 9 (6) (1997) 1591–1598.
[38] S. Sen, S. Mittal, G. Biswas, Flow past a square cylinder at low reynolds numbers, International Journal for Numerical Methods in Fluids 67 (9) (2011) 1160–1174.
[39] A. Pantokratoras, Steady flow of a power-law non-Newtonian fluid across an unconfined square cylinder, Journal of Applied Mechanics and Technical Physics 57 (2) (2016) 264274.
[40] N. Nirmalkar, R. Chhabra, R. Poole, On creeping flow of a Bingham plastic fluid past a square cylinder, Journal of Non-Newtonian Fluid Mechanics 171 (2012) 17–30.
[41] R. P. Bharti, R. Chhabra, V. Eswaran, Steady flow of power law fluids across a circular cylinder, The Canadian journal of chemical engineering 84 (4) (2006) 406–421.